12-15-2021 1:00 PM

Composite Compression Co-moulding: a Warpage Reduction Investigation

David Knezevic, *The University of Western Ontario*

Supervisor: Tutunea-Fatan, O. Remus, *The University of Western Ontario*
A thesis submitted in partial fulfillment of the requirements for the Master of Engineering
Science degree in Mechanical and Materials Engineering
© David Knezevic 2021

Recommended Citation

Knezevic, David, "Composite Compression Co-moulding: a Warpage Reduction Investigation" (2021).
Electronic Thesis and Dissertation Repository. 8333.
https://ir.lib.uwo.ca/etd/8333

Abstract

To accommodate the increasing need for vehicle emission reduction, automotive manufacturers are presently looking at the next generation of lightweight materials. Glass fibre-reinforced thermoplastic composites belong to this group and exhibit mechanical properties that resemble traditional metals but at a reduced weight and with improvements on other characteristics. Unfortunately, they are affected by processing-related warpage, especially when fabricated by means of the Long Fibre-reinforced Thermoplastics – Direct (LFT-D) manufacturing process, a technology that is valuable because of its high throughput and flow lengths. This occurs for many reasons but reinforcing LFT-D with Glass Mat Thermoplastics (GMT) – another material format with higher fibre content and isotropy – may overcome these issues altogether.

To validate this hypothesis, a complex demonstrator geometry was first selected. Then, the moulding of LFT-D was examined via thermography and moulding simulation to find thermal related issues caused by the geometry and material. Following this investigation, LFT-D was co-moulded with GMT and the resulting warpage was compared to both LFT-D and GMT by means of a deformation energy-based warpage metric as well as an image correlation metric used for warpage pattern similarity assessment. Nearly 25% LFT-D volume replacement with GMT provided warpages similar to the base GMT material with minimal changes to the warpage pattern. Though, subsequent mechanical tests yielded inconclusive results – most likely due to the confounding effect of specimen warpage – the overall results suggest a good bonding, fusion and mixing of the two co-molded materials. Further investigation of other warpage reduction methods could be considered in the future.

Keywords

Summary for Lay Audience

Due to pressure from climate change and governments, automotive companies are looking for lightweight materials capable of improving vehicle driving range. Materials such as glass fibre-reinforced plastics can have strengths comparable to steel and aluminum, but at a fraction of the weight. However, because of material design and the nature of manufacturing with these materials, they tend to deform from their designed shape – called warpage – leading to many downstream manufacturing issues. This work will explore the possibility of reinforce a material that is prone to warp, namely Long Fibre-reinforced Thermoplastics – Direct (LFT-D) process with another material, Glass Mat Thermoplastics (GMT) to reduce the overall part warpage.

To do this, first the moulding of selected components using LFT-D was looked at, and several temperature-related inconsistencies were expectedly found, as these are possibly the largest contributor to warpage. Then LFT-D was moulded together with GMT and the resulting warpage was measured and found to be much lower than LFT-D on its own and quite close to GMT on its own. This overcame the temperature issues amongst other warpage causes and demonstrated the success of the method. To further validate the method, the strength of the materials was tested to ensure that they bonded properly during moulding, and the cross-sections were examined under a microscope. Both tests showed promising results, but the sample size was too small to make a fully justified conclusion. Thus, further work on this topic is legitimized and shows that co-moulding may be a favourable technique for manufacturers.

Acknowledgements

First and foremost, I would like to acknowledge Dr. Remus Tutunea-Fatan for his role as my advisor. Without his guidance and outstanding support, I am not sure I would have made it to this point. From my first interaction with him in his 3rd year course, to coming to him for career advice, to working with him in a research assistant capacity, to a bachelor's thesis, and now a master's thesis, Dr. Tutunea-Fatan has been one of the biggest sculptors of the engineer I am today. With the many roles he plays at Western and his constant availability for questions and support, I'm not sure he ever sleeps. I truly wish everyone could have an experience like mine with Dr. Tutunea-Fatan.

Next, I would like to thank Navraj Heer, Dr. Stanislav Ivanov, and the rest of the staff the Fraunhofer Project Centre respectively, for their expert advisory related to the experimental and technical aspects of composite manufacturing and testing. Their help in organizing manufacturing trials and gathering data allowed for the successful accomplishment of this work.

Further, I would like to acknowledge Dr. Ryan Gergely, David A. Okonski, and General Motors of Canada for their collaboration, advisory, and funding, which have allowed for this project and others before it to be conducted and explored.

At Western there were many who helped this project at various stages. Thank you to Dr. Andrew Hrymak for leading this investigation into composite materials and providing your wisdom and funding opportunities to myself and my colleagues. Thank you to Dr. Dominik Dörr for your assistance and advice at almost every phase in this project, you've been a massive help to myself and my colleagues and I am sure we all greatly appreciate you. Thank you to Ivan Barker and Surface Science Western for their help in specimen imaging, they really are the best in the game. Thank you to the others on my advisory committee and examiner committee in Dr. Jeff Wood, Dr. Robert Klassen, and Dr. Daniel Langhor for your time and assistance in completing my degree. And to all my friends, family, and others at Western including my colleagues and supervisors in other capacities, I will always be grateful for your help in making my time here at Western as memorable as it was.

Thank you all.

Tables of Contents

List of Tables

List of Figures

List of Abbreviations

ANOVA	Analysis of Variance
DoE	Design of Experiments
FRP	Fibre-Reinforced Polymer
GFRP	Glass Fibre-Reinforced Polymer
GMT	Glass Mat Thermoplastic
LFT	Long Fibre Thermoplastic Composite
LFT-D-ILC	Long Fibre-reinforced Thermoplastics – Direct – In-line Compounding
SBI	Seat Back Inner
SBO	Seat Back Outer

Chapter 1 : Introduction

1.1 Overview

This introduction will provide the reader with the background necessary to understand the subsequent work in reduction of warpage in composite materials. Information will be presented which relates to thermoplastic composites and their manufacturing, warpage and connected topics, moulding simulation, data collection techniques related to thermal behaviour and warpage, and finally material characterization. Further, the motivation and objectives of this work, and contributions to the field will be put forth.

1.2 State of the Art/Literature Review

1.2.1 Thermoplastic Composites and their Manufacturing

Fibre-reinforced plastic (FRP) composites can be split into two groups based on the crosslinking of the polymer used. Crosslinked polymers are known as thermosets and are irreversibly chemically bonded during curing. Polymers with no crosslinking are known as thermoplastics and will liquefy above melting temperatures, making recycling possible as well. Thermoplastics are further split into amorphous and semi-crystalline varieties, with the latter exhibiting a nucleating behaviour at a crystallization temperature wherein polymer chains neatly fold themselves, but only to a certain degree unlike metals, hence the semi-crystalline [1].

Mass-manufacturing methods for such materials is possible in a variety of methods such as injection moulding, blow moulding or gas/water assisted injection, and compression moulding using Long Fibre-reinforced Thermoplastics – Direct (LFT-D) extrusion, Glass Mat Thermoplastics (GMT), or Light Weight Reinforced Thermoplastics (LWRT) material formats. However, the compression moulding of LFT-D and GMT materials are more

attractive primarily due to the possibility of higher discontinuous fibre lengths, a factor correlating to material strength [2]. The LFT-D process, but more specifically, LFT-D with In-Line Compounding (LFT-D-ILC) is depicted in Figure 1, wherein it begins with the heated compounding of the polymer along with possible additives in a twin-screw extruder to homogenize the mixture. The mixture is fed into a subsequent twin-screw extruder wherein fibres are chopped to length and incorporated into the polymer mixture. Once homogenized, the composite mixture is extruded through a die and cut to size, now constituting a 'plastificate' or 'charge', the semi-finished product immediately ready for compression moulding [3]. The charge fibres have a 3-D structure induced by the twin-screw rotation [4].
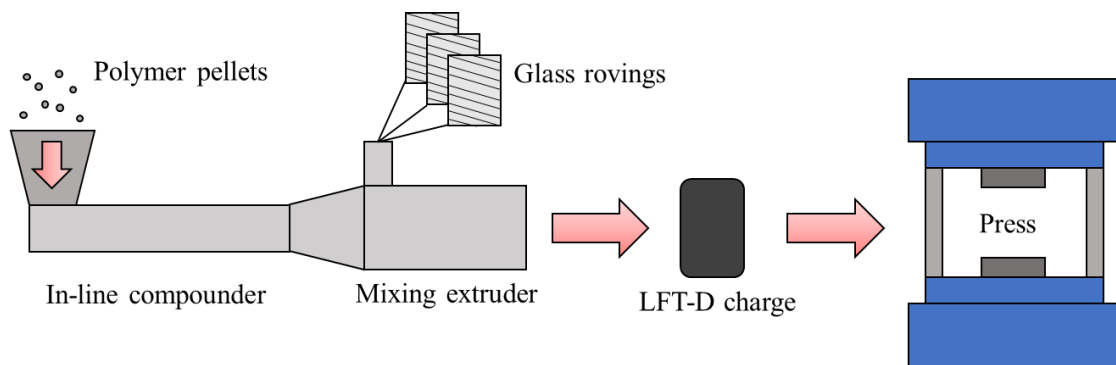
Figure 1: LFT-D-ILC process diagram

The creation of GMT products are generated somewhat more simply, involving only the impregnation of a mat of chopped and randomly oriented glass fibres with a thermoplastic [3]. The material is then cut and solidified and now constitutes a sheet, the semi-finished product which must first be reheated prior to compression moulding. In either case, the semi-finished product is then placed on a heated mould and compressed using high pressures to fill the desired geometry.

1.2.2 Warpage of Thermoplastic Composites

1.2.2.1 Causes of Warpage

In thermoplastic polymers and composites, part warpage can occur in several mechanisms. The most common process is via unequal thermal shrinkage and is best understood through a simplified format of a pressure-specific volume-temperature graph for semi-crystalline thermoplastics in Figure 2. As the material cools from processing temperature there is a general decrease in volume a sharp decrease at the recrystallization temperature, at which point the polymer chains nucleate into neatly packed crystals [5-7]. If for some reason cooling occurs at different rates within a part, the unequal shrinkage can cause deformation [8]. For example, a composite sheet being cooled at different rates on each side will cause the cooler side to contract faster than the hotter, leading to a curved geometry [9, 10].
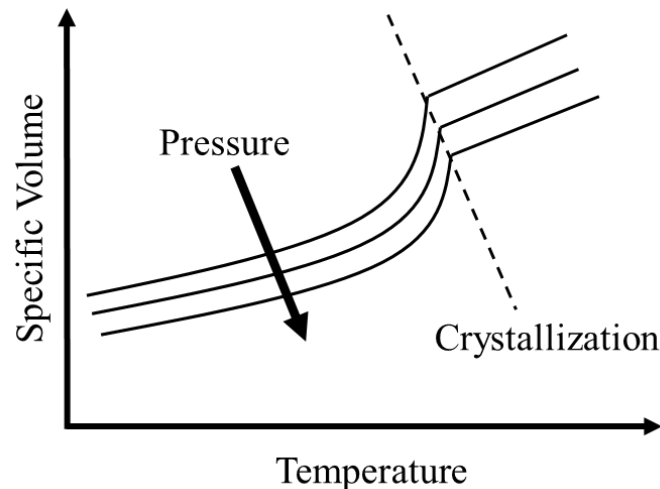
Figure 2: Simplified PvT graph of semi-crystalline thermoplastics

Warpage is also highly dependent on mechanical properties of the material. Particularly in composites, the difference in coefficients of thermal expansion (CTE) between the

constituents gives rise to residual stresses during cooling and contraction, leading to unequal volumetric shrinkage of each, thus causing cause warpage [11]. The level of anisotropy in the material also gives rise to residual stresses as the material may have directional variability in properties such as CTE, again leading to unequal shrinkage [11, 12]. This can arise from intentional orientation of fibres (i.e. unidirectional layups) or process induced orientation which orients fibres and polymer chains along the direction of flow during compression and mould filling [3, 12]

Apart from cooling rate and flow-effects, other processing conditions may influence part warpage as well. This includes: pressure, which can be seen through the volume dependency on pressure in Figure 2 [13-15]; hold time, which intuitively constrains warpage until temperatures homogenize [13-15]; mould temperature, which controls the eject temperature and post-mould cooling [9, 11, 15]; demolding method, which can impart stresses on the part [16]; and humidity, which for nylons relates to moisture absorption and changes in volume and mechanical properties [17, 18]. As a result, great care must be taken to create a repeatable process, and for industrial uses it may be of benefit to adopt a method by which these warpage causes can be mostly bypassed, i.e., further reinforcement.

1.2.2.2 Warpage Reduction Techniques

By understanding the various causes of part warpage, methods by which it can be reduced can then be explored. Perhaps the first technique that should be attempted is tuning of process parameters such as pressure, mould temperature, and hold time. In many studies this has been shown to be able to reduce the magnitude of warpage [13-15, 19, 20], however, past studies with the parts used in this work have been inconclusive in this venture [21]. Modification of the mould or part design to counteract the warpage direction is another viable option for

manufacturers and typically relies on both molding simulation and trial and error [22, 23]. Due to the iterative nature of this method, it can be inaccurate, financially burdensome, and can create significant production timeline issues. Annealing of parts post-moulding to relax residual stresses and therefore warpage can also be done, but faces similar issues in time, cost, and additional manufacturing floorspace, and is not as straightforward with anisotropic materials as it would be with isotropic ones [11, 24, 25]. Adding certain fillers to the matrix such as silica can narrow the differences of CTE between the fibres and matrix and substitution of matrix material to one with a lower glass transition temperature, T_g, can mitigate warpage by decreasing the difference in stress-free temperature and ambient thereby reducing residual stress [25]. While this may work in some cases, changing the matrix or formulation may not be feasible as they may be required for other purposes such as fire, chemical, or UV resistance.

Lastly, reinforcement of composite materials to increase strength and stiffness thereby reducing warpage has been shown to be an intuitive and successful method typically done with local reinforcements such as filament windings or unidirectional tapes [3, 26, 27]. Reinforcement of composites has also been successful in improving properties using organosheets [28], a material similar to GMT and easier to process compared to tapes and other local reinforcements. As mentioned, GMT allows for glass fibre weight fractions typically in the range of 60%, while compounding techniques like LFT-D only allow for as high as roughly 40% due to increasing fibre attrition from fibre-fibre and fibre-equipment interactions [29-31]. Thus, reinforcement of LFT-D to improve increase part fibre content and decrease warpage while maintaining flow-length capabilities and cycle time could be a robust technique for manufacturers.

1.2.2.3 Warpage Measurement and Metrics

Capturing geometric data from manufactured components can be performed in multiple ways. In industry, quality engineers typically assess data recorded by a physical probe on a coordinate-measuring machine (CMM). While contact CMM has its industrial uses, for purposes of reverse engineering and measuring deviation in a quasi-continuous fashion rather than at discrete locations, it is not feasible or even possible in some instances [32, 33]. As a result, non-contact measurement techniques have been developed to better serve these purposes, including 3D laser scanning. While 3D scanning is not as accurate as contact CMM [34-36], overall accuracy is dependant on user skill, component geometry, and surface finish, i.e., matte, glossy, reflective. Martin et al have conducted extensive work on this topic for the specific components used in this work and thus their methods will be followed [21, 37].

Evaluation of the collected data remains a complicated matter and is done again on a case-by-case basis. The geometry, application, and available measurement tools must all be considered when selecting an appropriate metric as simple metrics like change in length may not be relevant for complex or 3D geometries and may not be conducive to the application of the component. However, in literature, simple parts and metrics are often used to better quantify other experimental objectives. Some examples include the deflection of the bottom face of a bowl [9], waviness profile of a flat plate [14], in-plane and through-thickness shrinkage of a plaque [15], and spring-in of 'C' and 'L' shaped parts [38]. Previous studies using the more complex parts employed in this work used laser light probe scanning to digitize the parts to examine other metrics such as global deviation averages, region of interest deviation averages, and mating point deviation [37]. While they provided more information about the severity and behavior of part warp, they still suffered from data masking by way of

averaging tens of thousands of probe points. Also unrealizable with these methods is the correlation of geometric stiffness with warpage, i.e., two regions may exhibit the same deviation, however, one may have stored much more residual load due to a higher second moment of inertia. Thus, it may be beneficial to continue further in this venture to develop a more holistic representation of part warp.

1.2.3 Thermographic Imaging of Compression Moulding

In general terms, it is important to assess the thermal behaviour of components made in a thermo-forming process in order to better understand manufacturing related phenomena and the effects of various parameters. Moreover, this understanding is also important in understanding the causes and formations of part warpage. Specifically, any observed temperature gradients or localized anomalies could be key origins of warpage. One popular method for measuring and recording of temperatures induced by manufacturing processes relies on the use of a thermographic or infrared (IR) cameras that can fulfil various roles such as: i) measuring the increase of part and mould temperatures as a function of moulding cycle [39], ii) measuring part temperatures for closed loop control and diagnosis of quality and mould issues such as short shots, unbalanced injection, and low coolant temperatures [40], iii) visualizing mould filling behavior [41], and iv) validating simulated mould temperatures [42]. Thermography has also been used in compression moulding to better understand the induction heating of dies [43]. Despite its prevalent usage, there are limitations to its deployment and accuracy which are exacerbated by complex part geometries. The view angle has an inverse effect on the apparent temperature of non-conducting materials due to the angular dependency of emissivity [44-47]. The configuration used in this work can be seen in Figure 3. Because of this known error, the data is better evaluated on a relative, rather than absolute scale.

Nonetheless, since actual/absolute temperatures are of interest, it is also valuable to understand the angular characteristics of the camera. Based on experiments employing several different cameras in literature, the angle at which measurements begin deviating beyond 2% is approximately 60° [45, 46, 48], whereas more liberal estimates suggest this angle is around 70° [47]. Thus, the temperatures to be measured in the context of this study are not expected to deviate by more than 2% from their absolute values. Though, care must still be taken when interpreting data as depending on the geometry, certain faces may tend to reflect infrared radiation from adjacent faces [47], skewing values higher than expected.
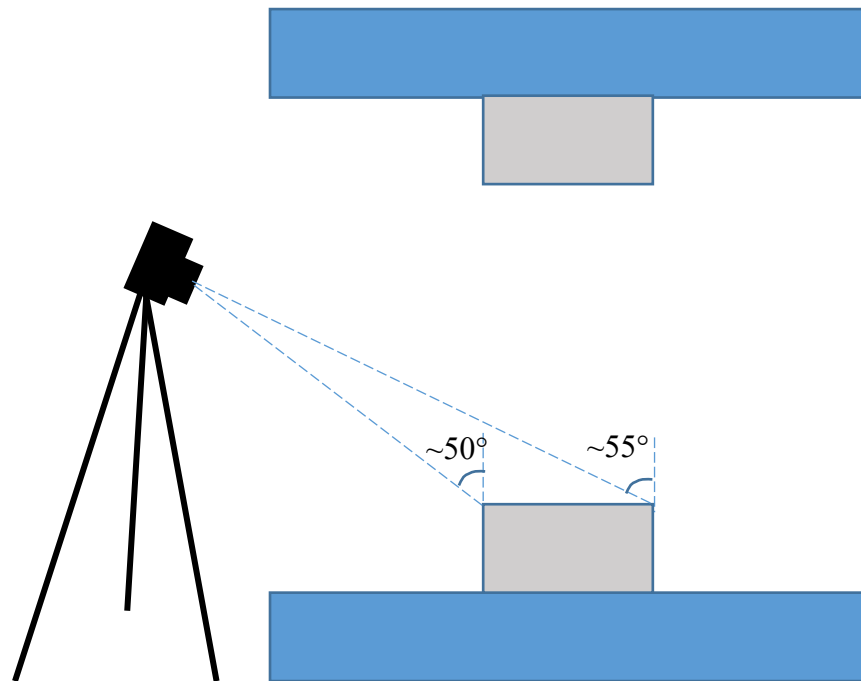
Figure 3: Camera view configuration with respect to moulding setup

1.3 Motivation

Composite materials – more specifically FRPs and glass fibre-reinforced plastics (GFRP) – have existed since the early to mid 20th century. Being a newer material in comparison to metals, ceramics, etc., there have been substantial advancements in material properties and

manufacturing methods such that their cost is now justified for use in high volume automotive products for everyday consumers. Instances of FRP material use in vehicles are well documented, however, with the emerging trend of reduction of emissions for economical reasons, the necessity for climate change, and looming government policies [49], vehicle lightweighting has been a principal issue for manufacturers in recent years [50]. Since FRP materials are typically less dense and characterized by similar strengths and improvements in other properties when compared to their metal counterparts, they became prime candidates for vehicle weight reductions [51]. Thermoplastic composites have seen an increased usage since the 1980's across the automotive and aerospace sectors due to their increased toughness and decreased cost when compared to their thermoset counterparts [2].

Accordingly, this project involves the use of glass fibre reinforced nylon 6 (polyamide 6) – a thermoplastic composite – for use in the automotive sector, and specifically of interest to General Motors. As a smaller part in a bigger scheme of advancing the state of simulation for composite processing, this project has used a physical demonstrator component in the form of a semi-structural seatback outer and inner assembly, depicted in Figure 4. These components are geometrically complex compared to many of those in literature, featuring ribs, channels, fillets, deep draw pockets, flanges, changes in thickness, and relatively large overall dimensions at approximately 550 x 480 x 100 mm, such that warpage issues are not simple to investigate or quantify.
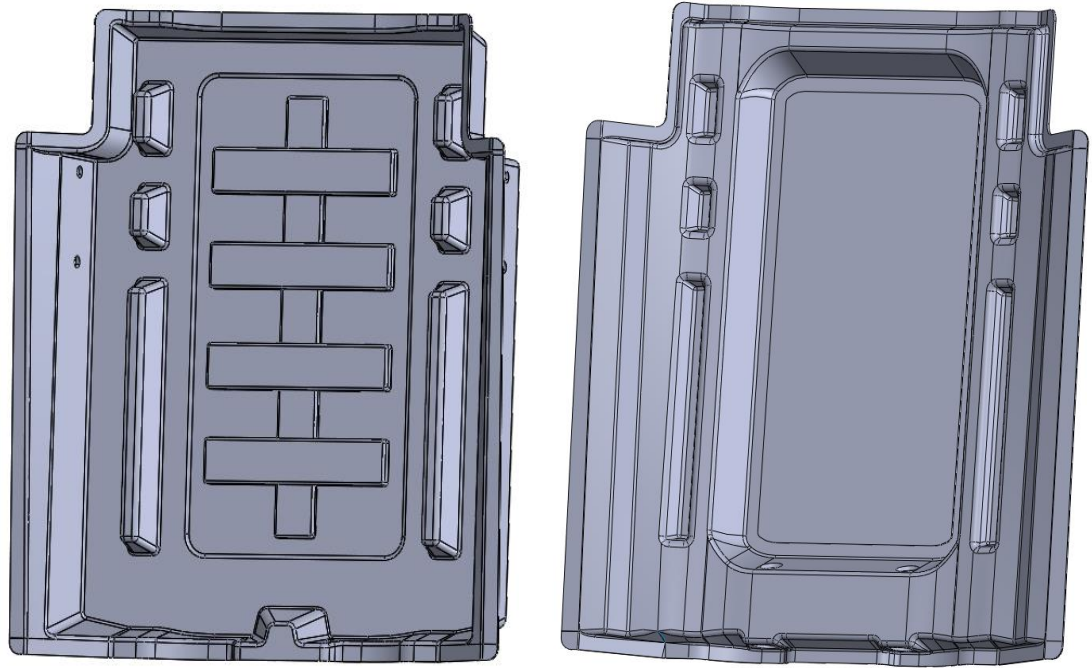
Figure 4: CAD model of demonstrator seatback outer (left) and inner (right)

In prior studies involving these parts [21, 37, 52], it was found that the components deviated by more than 10 mm in some locations when manufactured using LFT-D, and less than 5 mm in the same locations when manufactured using GMT. As explored in the previous sections, this is an expected observation due to the higher fibre content possible in GMT as compared to LFT-D, 60% by weight and 40% respectively, alongside the higher isotropy and lower flow lengths of GMT. Nonetheless, difficulties with mould filling were also present when GMT only was used. While this high level of warpage associated with the LFT-D process is undesirable and undermines the subsequent assembly and in-car performance via fracture and stress pre-load respectively, the process remains of interest due to its turn-key nature, flexibility and customization, rapid cycle time, and high flow lengths. These criteria are necessary for mass manufacturing of complex geometries, so much so that efforts to reduce warpage are warranted and welcomed. Thus, this project will examine the results and effects

of reinforcing LFT-D with GMT, with an overall goal to reduce part warpage. It is expected that the part warpage and mechanical properties will improve, and the co-moulded materials will still support filling of complex geometries.

1.4 Research Objectives

To investigate the warpage of these components and the possibility of co-moulding LFT-D and GMT to resolve the given issues, a list of objectives will be explored. Considering the complexity of GFRP materials, the required methodology must be holistic in nature for the proposed solution to be valid as changes to manufacturing can drastically alter properties and performance. Thus, the following objectives will be targeted throughout the proposed research project:

- Analyze the compression moulding process of LFT-D for insight into warpage behaviour, severity, and possible mitigation solutions.
- Manufacture co-moulded seatbacks with LFT-D and GMT and assess the results with an appropriate warpage metric.
- Review the feasibility/performance of co-moulded materials through mechanical testing and optical imaging of cross-sections.

1.5 Contributions

Based on the objectives set out, the following research contributions have been made:

- The development of thermal analysis techniques for compression moulding including: correlation of thermographic, sensor-acquired, and simulation data. Several recommendations will be made on the limitations of thermography when used on complex geometries.

- A study assessing the affects of processing parameters on eject temperature in a full-scale industrial manufacturing setting has been carried out and its conclusions were outlined.

- A new deformation energy-based warpage metric has been proposed. This summative metric also accounts for geometric stiffness, especially important for complex geometries.

- The warpage and mechanical properties of the new co-moulded material (LFT-D + GMT) were investigated and possible explanations for the observed abnormalities were proposed.

1.6 Thesis Overview

As a preface to the work conducted in this thesis, the following summaries of each chapter have been included. To aid in review, the respective summaries are also placed at the beginning of each chapter.

Chapter 2 aims to understand the thermal nature of composite compression moulding of LFT-D due to the deep correlation between temperature and warpage. The main objective of this study was to correlate thermography, physical sensors, and moulding simulation to further inspect conditions within the part and mould during and post moulding. Also conducted is an experiment using Design of Experiments which determines the significance of processing parameters on the temperature of parts upon ejection from the mould. This may provide insight into control of warpage severity.

Chapter 3 focuses on co-moulding of LFT-D and GMT. Once the warpage had been surveyed it was confirmed that co-moulding may in fact be a suitable robust method for warpage

reduction. Prior to this, a method for analyzing assembly of deformed parts was adapted to serve as an appropriate metric for quantifying warpage. Once established, manufacturing trials were conducted, and the warpage was compared between the base materials and co-moulded material. Since the seatback outer and inner share similar features and warpage behaviours, only the seatback outer was chosen for this study as the results would likely see comparable results with the seatback inner.

Chapter 4 provides further detail about the feasibility of co-moulding the same constituent materials in different formats. Here, the mechanical properties are tested to confirm that the materials are properly bonded and perform as expected. Optical microscopy is also used on several specimens to search for possible anomalies at the interface of the materials.

Chapter 5 is the conclusion of the thesis, wherein the key findings in each chapter are summarized and future work is discussed.

Chapter 2 : Thermal Analysis of Compression Moulding

2.1 Overview

Chapter 2 aims to understand the thermal nature of composite compression moulding of LFT-D due to the deep correlation between temperature and warpage. The main objective of this study was to correlate thermography, physical sensors, and moulding simulation to further inspect conditions within the part and mould during and post moulding. Also conducted is an experiment using Design of Experiments which determines the significance of processing parameters on the temperature of parts upon ejection from the mould. This may provide insight into control of warpage severity.

2.2 Methodology

2.2.1 Experimental Setup

The material used in this study was BASF Ultramid 8202 HS polyamide 6 (PA6) with 40wt.% Johns Manville glass-fibre. At the Fraunhofer Project Centre for Composite Research (FPC) in London, Ontario, charges of this material were compounded using the LFT-D process that output charges to the specific weight required to fill each respective part. They were approximately 350×100×45 mm in size for the SBO and 450×100×25 for the SBI. The cut charges were placed by an operator on one side of a shear-edged compression moulding tool and compression moulded using a Dieffenbacher 25,000 kN press. The trials for each of the two geometries were performed according to the parameters shown in Tables 1 and 2 to discern the effects of the given parameters on eject temperature in the following case study. Process parameters were varied according to the tables, and the resulting charge and part temperatures were analyzed.

Table 1: Factors and levels for SBO moulding trials

Factor	Level 1	Level 2
Hold Pressure	200 Bar	300 Bar
Hold Time	75 s	90 s
Charge Orientation (w.r.t. to mould)	Lengthwise centred	Widthwise centred

Table 2: Factors and levels for SBI moulding trials

Factor	Level 1	Level 2	Level 3
Mould Temperature	100 °C	125 °C	150 °C
LFT-D Temperature	280 °C	300 °C	-
Hold Time	45 s	60 s	75 s

An IR camera was mounted beside the mould to acquire the temperature of the charge as set on the core-side of the mould prior to compression and of the moulded part after compression. The camera used was a Fluke TiX580 characterized by 34° x 24° field of view, 640 x 480 pixel resolution, spectral band of 7.5μm to 14μm, and an accuracy corresponding to the greater of ± 2°C or 2% [53]. The arrangement was seen in Figure 3 with an angle between the normal of the mould surface and camera of approximately 50° to 55° for the near-side to the far-side of the mould, respectively. As mentioned, this angle has an inverse effect on apparent temperatures, meaning they may be observed to be lower than in reality. Since these angles are not above 60°, apparent temperature should not deviate more than 2%.

2.2.2 Moulding Simulation

2.2.2.1 Simulation Setup

To assist with the verification of experimental results and to set the premises for future work, Moldex3D was used to simulate the compression moulding process for comparison to experimental thermographic and thermocouple measurements. This commercial software allows for thermal flow simulations and includes a pre-processing and post-processing package. Thus, one set of moulding process parameters for each of the two parts was selected

for this purpose. The moulding process flow diagram is illustrated in Figure 5 and process parameters are summarized in Table 3 for the selected seatback outer (SBO) and seatback inner (SBI) runs. The material card used was created by Moldex3D and General Motors and kept confidential. The properties needed for simulation and the resulting material card were generated from compression moulded, linear-flow square plaques and the following modelling equations can be found in the Moldex3D technical reference [54]. Viscosity was modeled using the Cross-WLF model. PvT behavior was modeled using the 2-domain Tait model and crystallization kinetics used the Nakamura model. Structural viscoelasticity relied on the Generalized Maxwell model, and flow viscoelasticity used the Phan-Tien and Tanner model. Heat capacity and thermal conductivity were both tabulated up to 290°C. The coefficient of linear thermal expansion and mechanical properties were tested in both flow and cross-flow directions.
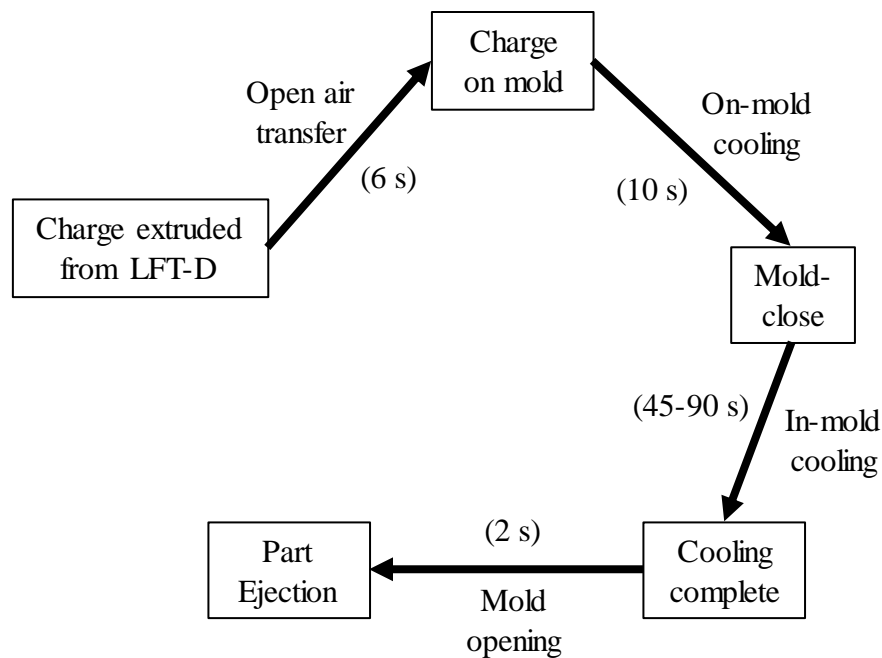
Figure 5: Flow diagram of the compression moulding process

Table 3: Trial parameters for simulation setup

Parameter	SBO	SBI
Mould Temperature	150 °C	150 °C
Charge Temperature	275 °C	295 °C
Holding Time	75 s	45 s
Force	7545 kN	7454 kN
Charge orientation	Lengthwise	Lengthwise
Max. closing speed	80 mm/s	80 mm/s

Some notable discrepancies were noticeable between Moldex3D simulations and manufacturing trials. In terms of root causes for these differences, it could be mentioned that the CAD models of the parts were initially difficult to mesh within Moldex3D (due to topological inconsistencies or inaccuracies). As such, the required removal of fillets and other minor details led to slight increases of the part volume. Furthermore, the actual CAD model of the mould used for the trials was unavailable. However, the software allowed a number of workarounds/simplifications that included the generation of the cooling channels. The set points of the upper and lower oil channels were 170°C and 165°C respectively. They were set to achieve an initial mould surface temperature of 150°C. The moulding configuration can be seen in Figure 6: outer box is the mould block, part cavity is in beige, the charge is in red laying across the length of the cavity, and the cooling channels with baffles are in blue. The cooling channels are locked into position in the simulation. This essentially means that the cooling channels in the upper tool half begin cooling the material immediately rather than cooling once the tool comes into contact with the charge. While this approach may cause some variance in the initial boundary conditions, it was deemed acceptable. The part mesh was constructed using boundary layer elements to better resolve the thermal fluid-flow and set to 5 layers of elements totalling nearly 620, 000 elements. The size of such elements was not alterable by the user. The compression zone above the part where the charge is allowed to flow was also set to a

boundary layer mesh and used only 3 layers as it was less critical for determining accurate part properties. The cooling channels featured 5 layers of hexa-based elements, and the mould block was a pure tetrahedral mesh, automatically generated and refined near the part, cooling channels, and compression zone. The element counts for components other than the part were not retrievable.
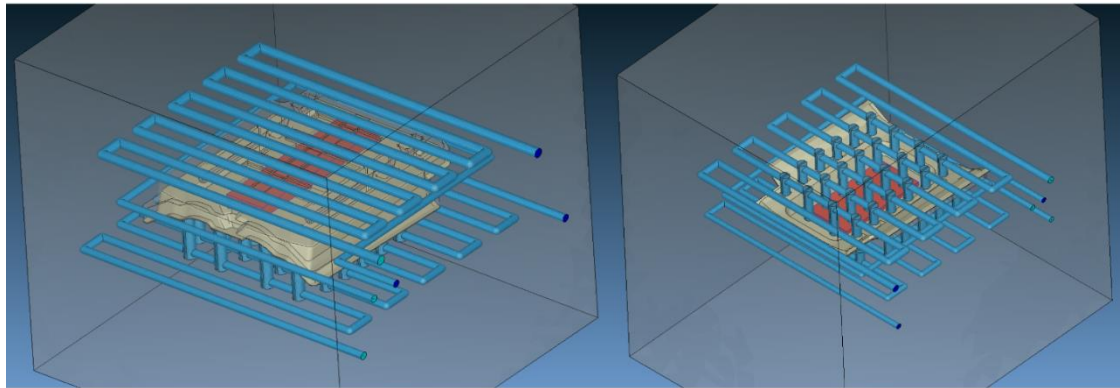
Figure 6: Moulding simulation configuration for SBO (left) and SBI (right)

Considering the charge would experience significant ambient air exposure time from the LFT-D extruder to mould-close (Figure 5), it was necessary to model the charge temperature evolution prior to moulding as this temperature highly influences mould filling and possibly ejection temperature. As such, the time the charge was exposed to air during processing was measured and hand calculations were used to approximate the charge temperature at mould close. Since Moldex3D is capable of modeling heat exchange as the charge lays on the mould, only the temperature after transfer between the LFT-D line and the mould was needed.

In order to determine the initial charge temperature for the purpose of compression moulding simulation, the charge was modeled using the lumped capacitance method [47], wherein the charge is assumed to have a near-uniform temperature distribution. This had to be assumed

since the conductivity of the charge is low and any thermal penetration during the time of air exposure will likely be contained to a relatively small penetration depth from the surface. The upcoming formulae are from Bergman *et al.* [47]. By modeling the charge as being carried through air at 1.4 m/s, the convective heat transfer coefficient was found beginning with the associated Reynold's number (Re):

$$\mathrm{Re} = \frac{uL}{v} \tag{1}$$

where u is the relative air velocity, L is the length of the charge surface, and v is the kinematic viscosity of air. This flow was determined to be laminar in both trials since $\mathrm{Re} < 5\times10^5$, and the following formula was used for the Nusselt number (Nu):

$$\mathrm{Nu} = 0.664\,\mathrm{Re}^{1/2}\,\mathrm{Pr}^{1/3} \tag{2}$$

where Pr is the Prandtl number of air. The convective heat transfer coefficient (h_C) can be found as:

$$h_C = \mathrm{Nu} \cdot \frac{k}{L_C} \tag{3}$$

where k is the thermal conductivity of air whereas L_C is the characteristic length of the charge defined as:

$$L_C = \frac{A_S}{P} \tag{4}$$

Here, A_S is the surface area and P is surface perimeter. The radiative heat transfer coefficient (h_r), was found using the following:

$$h_r = \varepsilon\sigma(T_S + T_{surr})(T_S^2 + T_{surr}^2) \tag{5}$$

where ε is the emissivity of the charge (0.89), σ is the Stefan-Boltzmann constant, T_S is the surface temperature of the charge, and T_{surr} is the temperature of the surroundings. Hence, the lumped capacitance temperature can be found by means of:

$$T(t) = T_\infty + (T_i - T_\infty)\exp(-\frac{hA_S}{\rho Vc}t) \tag{6}$$

where T_∞ is the surrounding temperature, T_i is the initial temperature, h is the sum of the convective and radiative heat transfer coefficients, ρ is the charge density, V is volume, c is specific heat capacity, and t is exposure time. The results for each case are presented in Table 4. The calculated temperature is then applied as the initial charge temperature and assumed to be homogenous throughout the charge. Subsequently, a 10 s pause time was simulated while the charge lay on the tool before the start of compression as measured during the trials.

Table 4: Values for charge temperature calculation

Variable	SBO	SBI
Charge dimensions [mm]	350×100×45.63	450×100×24.88
Re	16,896	20,322
Nu	76.19	83.56
h_C [W/(m²·K)]	68.55	56.48
h_r [W/(m²·K)]	16.74	18.57
T (t = 6 s) [°C]	275	295

2.2.2.2 Simulation Model

During the filling process in Moldex3D, the air and polymer melt are considered to be weakly compressible, and the polymer is described as a Generalized Newtonian Fluid (GNF) [54]. The non-isothermal material flow during the mould filling stage was modeled according the general principles of mass, momentum and energy conservation. To model the viscosity of the polymer, a modified-Cross model with Arrhenius temperature dependency was used:

$$\eta(T,\dot{\gamma}) = \frac{\eta_0(T)}{1+\left(\dfrac{\eta_0\dot{\gamma}}{\tau^*}\right)^{1-n}} \tag{7}$$

where n is the power law index, η_0 is the zero-shear viscosity, and τ^* is a parameter describing the transition region between the Newtonian plateau and the power law region. The zero-shear viscosity is described as:

$$\eta_0(T) = B\exp\left(\frac{T_b}{T}\right) \tag{8}$$

where B is the consistency index, T_b is a measure of the material temperature sensitivity, and T is the melt temperature. Finite volume method was employed to solve the 3D transient fluid flow, whereas heat equation was used to model the heat transfer through the mould during the transient in-mould cooling analysis. In addition to this, a convective boundary condition was applied to the inner surfaces of the cooling channels with the heat flux expressed as:

$$\dot{q} = h_f(T_W - T_C) \tag{9}$$

Here, T_W is the temperature at the mould cooling channel interface, T_C is fluid temperature, and h_f is the heat transfer coefficient calculated as:

$$h_f = \frac{Nu \cdot k}{d_0} \tag{10}$$

Here, d_0 is the wetted perimeter of the channel and Nu is the empirical Nusselt number:

$$Nu = 0.023\,Re^{4/5}\,Pr^n \tag{11}$$

where n is 0.3 for cooling.

Furthermore, the heat flux between charge/part and mould was specified as:

$$q = h(T_{mt} - T_{mb})$$ (12)

where T_{mt} is the mould-melt interface temperature, T_{mb} is the mould temperature, and h is the automatically generated heat transfer coefficient. Since the physical measurement of the temperature within the mould – performed with a thermocouple – yielded readings within 1.2°C with respect to their virtual counterparts within Moldex3D, the automatic software-based computation of the heat transfer coefficient was deemed sufficiently accurate.

For warpage. the material card was generated from the separated properties of the matrix and fiber as inputs to the Mori-Tanaka micromechanics model [54]. The warpage calculation begins once the mould has been filled, progresses through the cycle, and continues after the part is removed and allowed to cool to room temperature. The calculation considers fiber orientation and viscoelastic effects. The governing equations are then described as:

$$\sigma_{ij,j} + f_i = 0$$ (13)

where f_i is the body force and σ_{ij} is the stress components described as:

$$\sigma_{ij} = C_{ijkl}(\varepsilon_{kl} - \varepsilon_{kl}^0 - \alpha_{kl}\Delta T) + \sigma_{ij}^F$$ (14)

where C_{ijkl} is the elastic material stiffness, ε_{ij}^0 is the initial strain from PvT effect, α_{kl} is the coefficient of linear thermal expansion, ΔT is the temperature difference, σ_{ij}^F is the initial stress induced by flow, and ε_{ij} is the infinitesimal elastic strain component described by:

$$\varepsilon_{ij} = \frac{1}{2}(u_{i,j} + u_{j,i})$$ (15)

where $u_{i,j}$ and $u_{j,i}$ are displacement gradient.

2.2.3 Statistical Approaches

After thermographic video capture, selected frames were extracted for further statistical processing in a thermographic case study. More specifically, three images of charge or part temperature were exported in comma-separated values format and imported into to Matlab for statistical analysis. The three imaging instants were correlated with the moment when: i) the charge was is placed on the mould (outer charge temperature), ii) the mould is closing (outer charge temperature), and 3) the part is about to be ejected (part temperature). The thermal information of interest from both charge and part included the average temperature, standard deviation in temperature as well as pixel count. The direct application of this technique to ejected parts was accompanied by challenges caused by the similarity of temperatures for part and mould. Because of this, simple thresholding techniques could not be used to isolate the pixels depicting part temperature. To isolate the region of interest, a visual mask was applied to image data arrays such that only part data was extracted. The existence of this mask was facilitated by the fact that parts were ejected near the same spatial position for each compression moulding cycle. The three main image processing phases are illustrated in Figure 7.
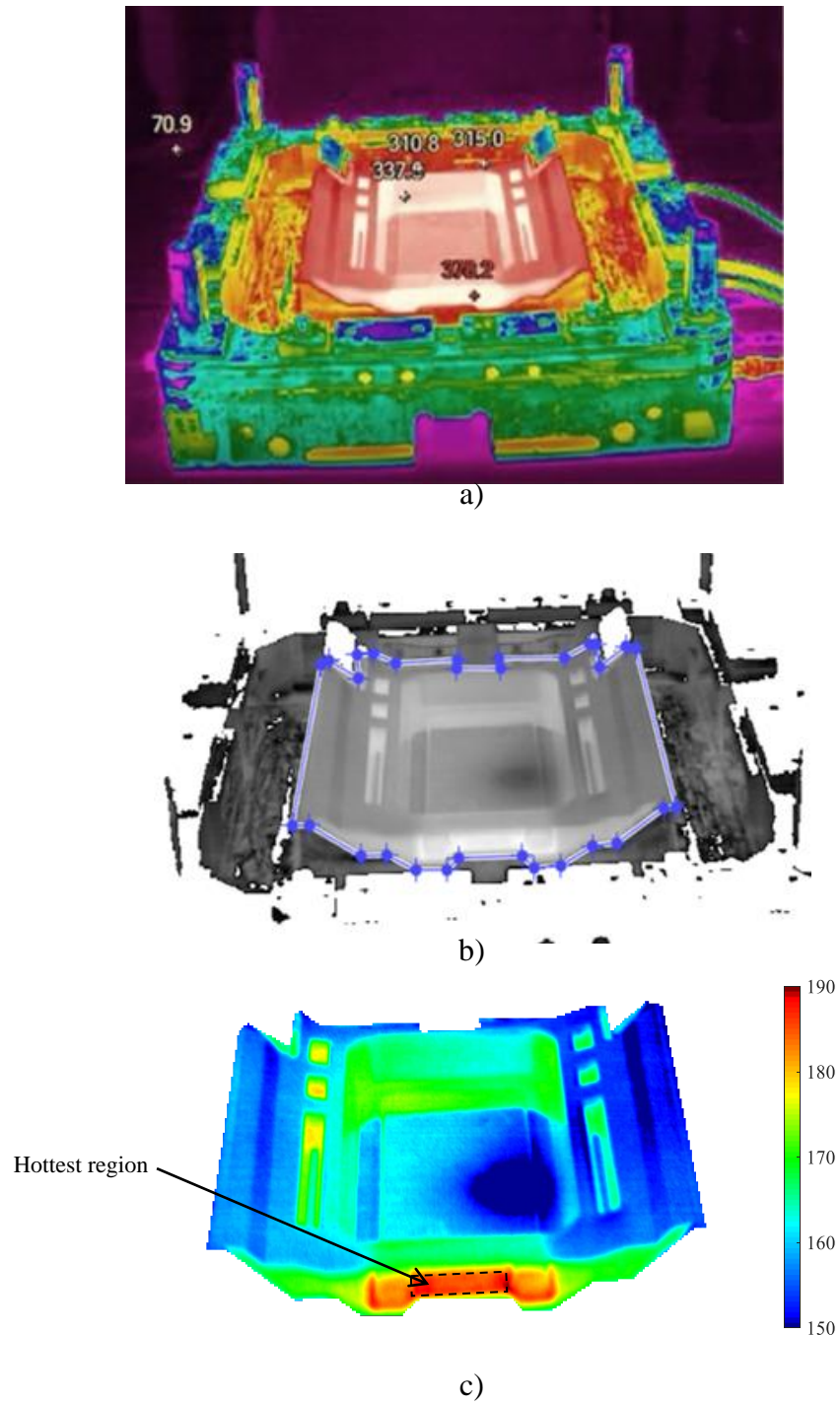
Figure 7: Image processing phases: a) raw IR image of a part after mould open (°F), b) SBI mask creation using polyline in grayscale and c) MATLAB temperature plot of ejected SBI part (°C)

To evaluate the effect that process parameters may have on ejection temperatures, ANOVA studies were performed with Minitab [55, 56], and each parameter was hypothesized to have an influence on the output variable of interest, namely: part temperature. The following considerations were accounted for: i) mould temperature sets a minimum for eject temperature, ii) LFT-D temperature sets a starting point for cooling within the mould, iii) pressure is known to increase temperature in polymers [57, 58], as well increasing thermal contact conductance, iv) holding time regulates how long a part is given to cool down, and v) charge orientation dictates flow length and thus possible cooling rate. Realistically, the charge temperature as the mould closed would be of more value than LFT-D temperature. Nevertheless, it was determined through a study to be explained in the upcoming Section 4.1 that LFT-D set point had a strong enough relationship with the final temperature of the charge ($p < 0.05$). Furthermore, the analysis is simplified by means of the LFT-D set point since it is a fixed and discrete variable, whereas the actual LFT-D charge temperature is continuously variable.

In both trials, a full-factorial experiment design was performed with all possible parameter combinations and at least five replicates for each run. The data for each replicate was imported into Minitab. It was ensured that the two conditions for accurate ANOVA test results were met: i) homoscedasticity of error variances (constant variance of residuals across the data; this was tested by means of the Levene test [55]), and ii) normality of data within sets (tested using the Anderson Darling test [55]). The deletion of some outliers was required to meet these criteria, often due to short-shots or the camera experiencing significant lag resulting in incorrect measurements.

2.3 Analysis and Validation of the Thermal Data

2.3.1 Thermography-Acquired vs Simulation-Yielded

Simulation of the compression moulding cycle yielded results that were partially consistent with the experimental trials and revealed important information about the thermal behavior of the material. The compression moulding cycle for a SBO was simulated using the parameters listed in Table 3. Simulated temperatures were exported by means of "probe points" and then compared with those yielded from MATLAB-processed images captured by the thermographic camera (Figure 8). A total of 42 points were used in this comparison and the summary of the results is presented in Table 5.

a)   b)
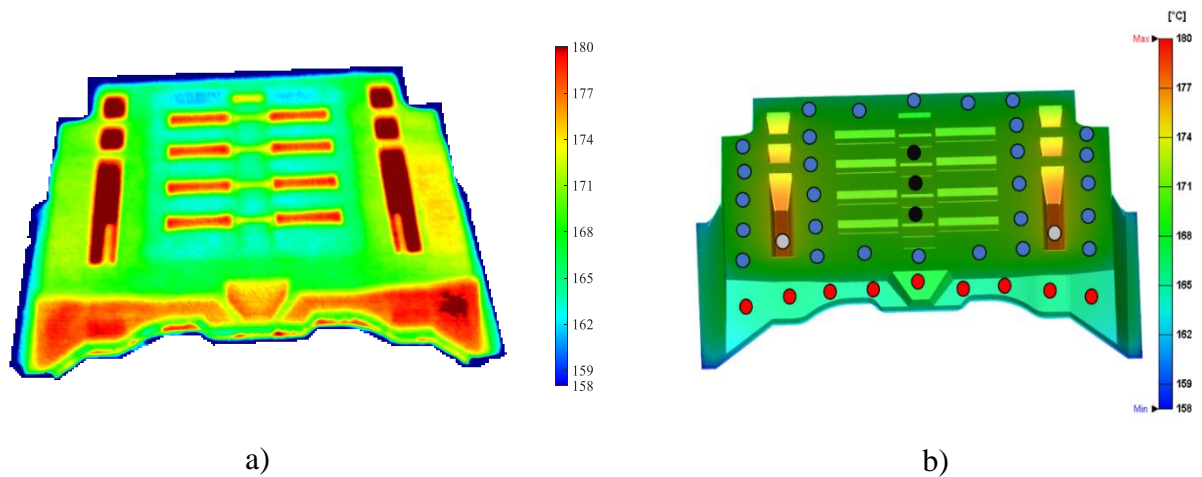
Figure 8: Comparison of SBO temperatures yielded from: a) infrared camera measurements and b) moulding simulation

Table 5: Comparison of simulated and measured temperatures for SBO
(error bars represent one standard deviation)

Probe Group	Color	Average Temperature (°C)		Number of Probes	Difference (%)
		IR Camera	Simulation		
Front face	Red	177.5 ± 1.5	165.9 ± 0.7	9	7.0
Top-most surface	Blue	168.6 ± 3.3	170.6 ± 1.3	28	-1.1
Deep draw pockets	Gray	175.5 ± 0.4	173.4 ± 0.0	2	1.2
Centre pockets	Black	163.7 ± 0.4	170.8 ± 0.1	3	-4.2

When analyzing this data, it can be noticed that while variations between simulation and direct camera readings are present, the results remain comparable. The aforementioned discrepancies can be attributed to a variety of sources of error such as camera accuracy ($\pm$ 2%), view angle (-2%) as well as typical assumptions that are characteristic to any moulding simulation. Moreover, the deep pockets are a source of more erroneous results due to the likelihood of reflections from adjacent and opposing walls. Because of this reason, they were largely excluded from probe comparison analysis. Similarly, the temperature measurements on the bottom face of the part (marked by red probes) are likely affected by inaccuracies due to the radiation caused by the lip of the heated mould base placed directly in front of it. More specifically, since the emissivity of the material is 0.89 and absorptivity is typically equal with emissivity that is experimentally determined at a given wavelength, the reflectivity of the material was calculated at 0.11 according to the following relationship for opaque bodies [47]:

$$\alpha_\lambda + \rho_\lambda = 1 \tag{16}$$

where α_λ and ρ_λ are the absorptivity and reflectivity at a given wavelength, respectively. Thus, only a small fraction of the incident radiation originating from the mould base would be reflected by the SBO surface. This is consistent with the experimental findings since the apparent increase seems to be of around 10-15°C. Furthermore, the existence of such sharp gradients between faces prone to reflection and those that are directly adjacent with no reflection suggests that the apparent temperatures on the faces prone to reflection are not real.

A similar analysis was conducted on SBI whose moulding cycle parameters are also listed in Table 3. A total of 39 temperature probes were used for comparison purposes (Figure 9 and Table 6). As it can be observed, while certain similarities between the temperature patterns of the two parts do exist, discrepancies are also present. For instance, the bottom face of the part (marked by yellow probes) is again much hotter than Moldex3D simulation predicts. Same as for SBO, this can be attributed to the same reflecting radiation from the lip of the mould base. Nonetheless, in case of SBI, the thermographic image tends to suggest lower temperatures than the ones yielded from the simulation. Unlike in compression moulding of SBOs, an air ejector was used to free SBIs from the top half of the mould and because of this, a clear circular spot can be seen in all parts. While the actual cause for this discrepancy will be investigated in a future moulding trial (to be conducted without air ejectors), it is possible that this temperature drop of several degrees was caused by a draft of cold air that passed over the part as it vented. According to the simulated temperature field, the highest temperature of 175°C was again noticed in the deep draw pockets but also the bottom section of the part, where the part is nearly twice as thick as the rest of the part. Same as for the SBO, simulation suggests that the temperature decreases radially outward towards the edges where the temperature reaches 158°C. However, the air ejector used in SBI moulding causes the lowest

temperature of the mould to drop at 150°C, thus creating a significantly larger temperature gradient across the part which presumably translated in large warpages.

a)   b)
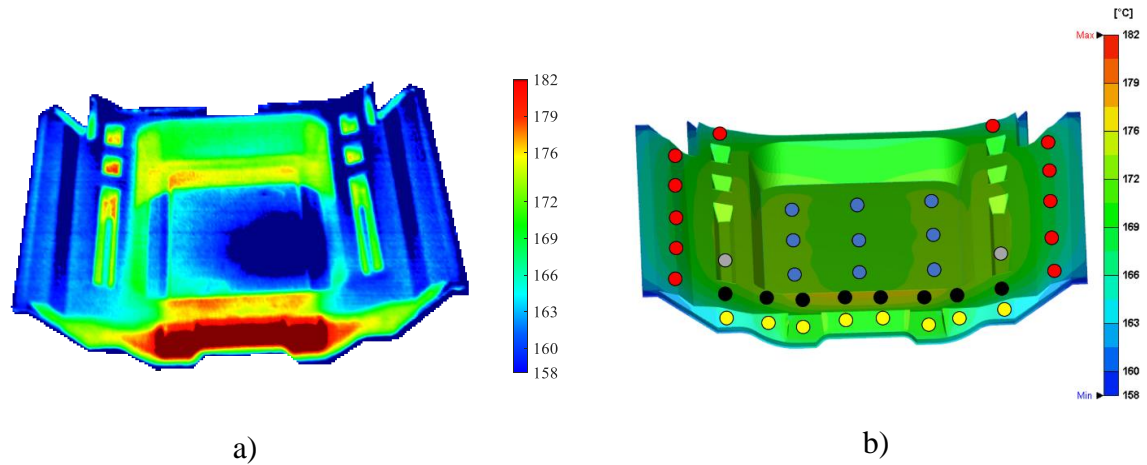
Figure 9: Comparison of SBI temperatures yielded from:
a) infrared camera measurements and b) moulding simulation

Table 6: Comparison of simulated and measured temperatures for SBI (error bars represent one standard deviation)

Probe Group	Probe Color	Average Temperature (°C)		Number of Probes	Difference (%)
		IR Camera	Simulation		
Bottom face	Yellow	181.4 ± 5.7	167.8 ± 1.6	8	8.1
Flanges	Red	159.2 ± 2.6	168.0 ± 1.5	12	-5.2
Deep Draw Pockets	Gray	163.7 ± 0.4	171.4 ± 0.1	2	-4.4
Back plane	Blue	160.2 ± 4.8	167.2 ± 0.3	9	-4.1
Lower front face	Black	169.7 ± 6.2	173.0 ± 2.3	8	-1.9

2.3.2 Thermography-Acquired vs Thermocouple-Collected

The surface mounted thermocouples provided another perspective in the comparison of thermography to simulation, and they assisted with the overall understanding of the compression moulding process. Their location within the mould is shown in Figure 10 and they feature an accuracy of ± 2.2 °C. The temperatures reported at end-of-cycle between the simulation and thermocouples are seen in Table 7. An appreciable similarity is observed, much more so than between thermography and simulation, providing another layer to the validity of simulation.

a)

b)
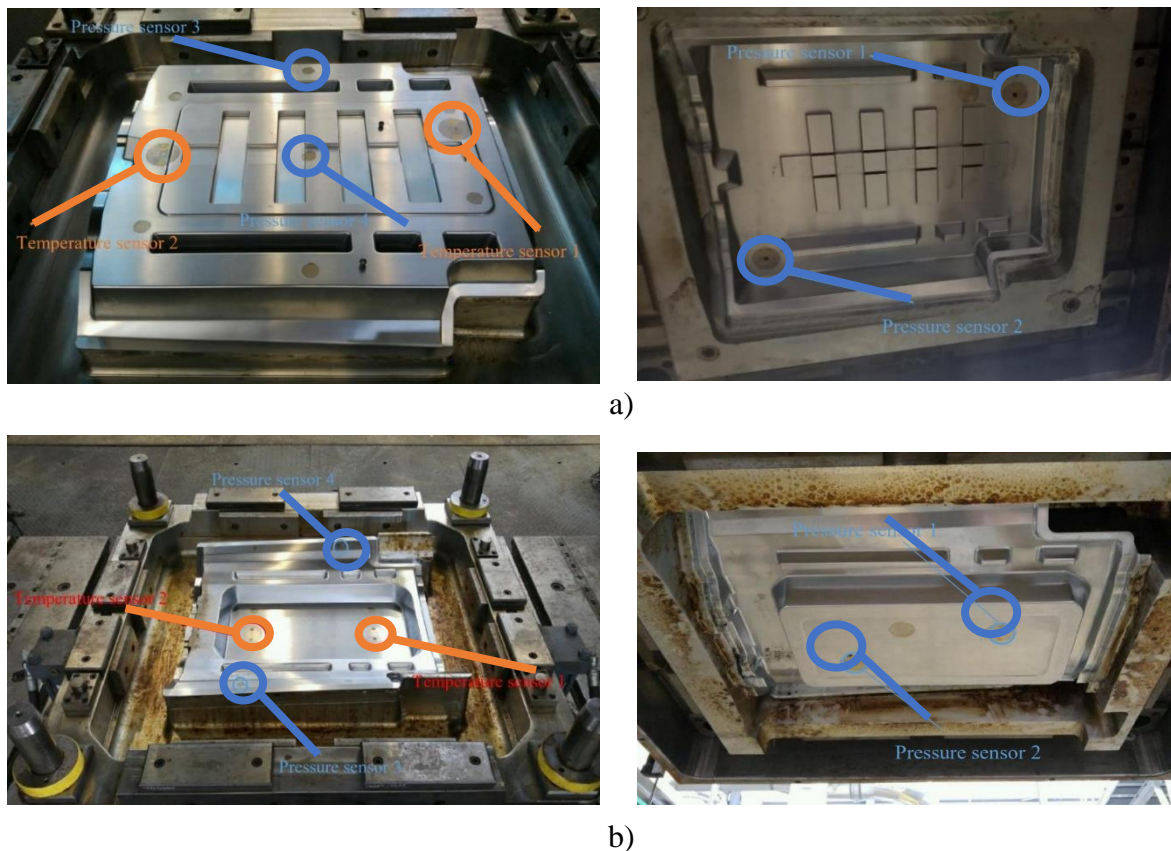
Figure 10: Mould halves with sensor locations highlighted in blue (pressure) and orange (temperature) for: a) SBO and b) SBI

Table 7: Comparison of mould-mounted thermocouple (TC) sensors to probes in Moldex3D simulation

Geometry	Comparison	Temperature (°C)	Delta (°C)	% Difference
SBO	TC1	170.4	-1.2	0.7
	Simulation Probe	171.6		
	TC2	170.1	3.4	2.0
	Simulation Probe	166.7		
SBI	TC1	166.4	-0.9	0.6
	Simulation Probe	167.3		
	TC2	164	-4.1	2.5
	Simulation Probe	168.1		

Shown in Figure 11a is the part ejection temperature, and the temperature of the two in-mould temperature sensors for the first series of six parts moulded sequentially in the trial. The data shows that as the mould temperature increases, so does the ejection temperature. This is most likely caused by the quick moulding cycle that is characteristic to thermoplastic moulding: mould heating is caused by the introduction of the next hot charge. Because of this permanent additional influx energy, the process cannot reach the thermal equilibrium for a certain amount of time. In case of trials performed within the scope of the present study, ejection temperatures varied by at least 2°C within the same set of process conditions at the point of quasi-equilibrium. This implies that a true thermal equilibrium was not reached. A direct consequence of using moulding conditions that are outside of the stable thermal regime would be the necessity to scrap a number of initial parts that were produced before the equilibrium conditions were achieved.
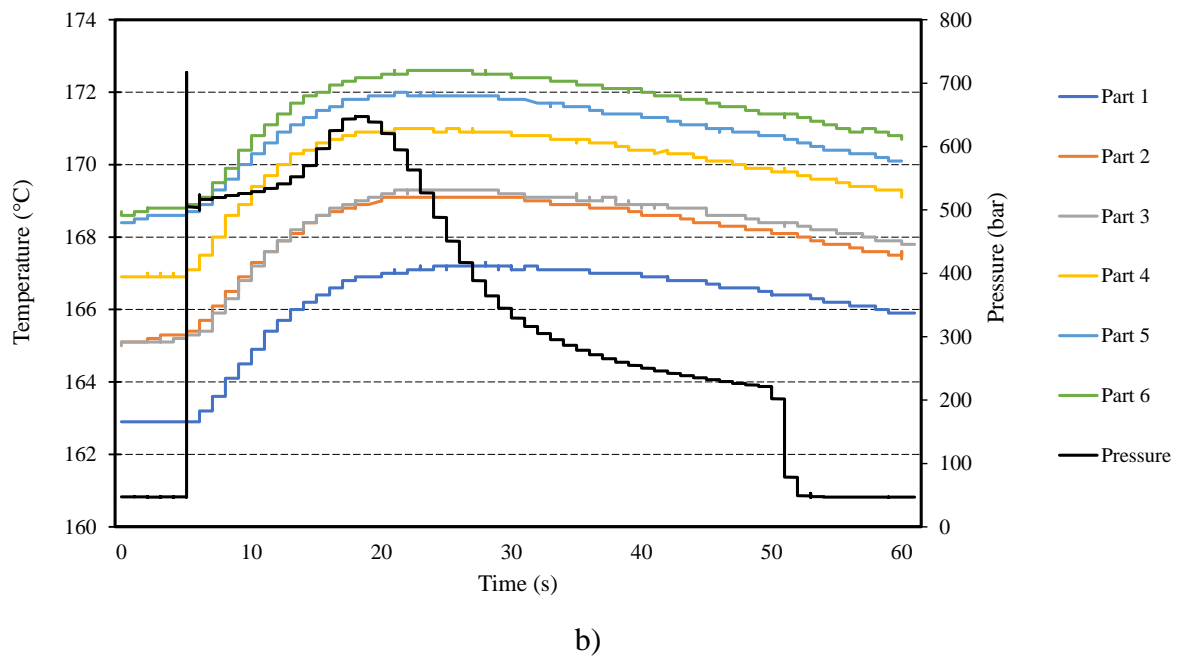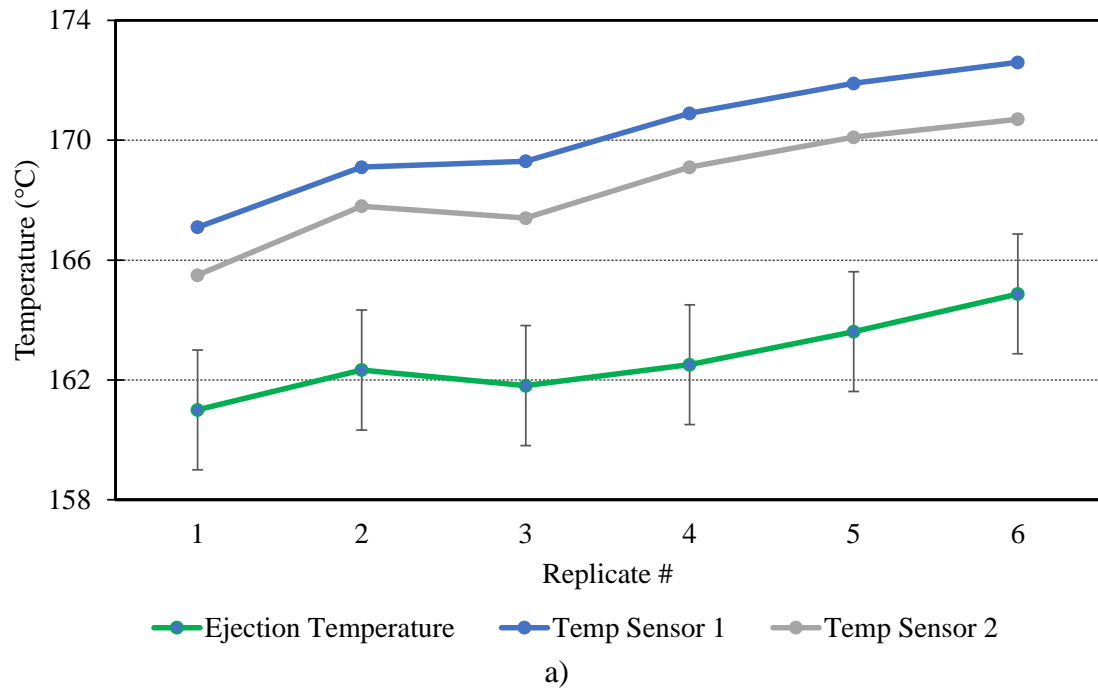
Figure 11: Correlations between mould temperature sensor data and: a) part ejection temperature (error bars represent camera accuracy) and b) mould pressure sensor (data presented for the same set of SBI parts)

The typical pressure response of the sensors compared to the temperature response is depicted in Figure 11b. The plot outlines a distinct rise in mould temperature as pressure is applied to the charge followed by slow drop towards the end of the moulding cycle. The temperature rise can be explained through the reduction of thermal contact resistance between two surfaces with applied pressure [47], as well as – albeit to a lesser extent – through to the pressure heating of polymers that are a weak compressible substance [57, 58]. The drop in temperature towards the end of the moulding cycle is caused by mould cooling.

2.3.3 Discussion and Warpage Insights

In light of the occasionally contrasting results between simulation and thermography – most likely caused by the radiative/reflective effects of the adjacent hot surfaces – one of the primary suggestions to be made is to carefully monitor/scrutinize for environmental factors that might confound the precision of the thermographic measurements. This is particularly relevant in the industrial context in which the overall configuration of the experimental setup does not always allow for an optimal placement of the thermographic camera. With the exception of certain areas that are negatively influenced by reflection in the thermography results, it could be asserted that thermography, thermocouple and simulation yield comparable temperature measurements and/or predictions.

Given the amount of possible error in the thermographic images, it is not suitable to extract conclusions about absolute temperature behavior. However, the relatively good accuracy of the moulding simulation allows for such conclusions to be drawn and suggests that temperature gradients up to 20 °C can exist across the entirety of the parts. This thermal dissimilarity is a commonly accepted cause of warpage and it is believed to occur via the entrapment of heat in the numerous cavities created by deep draws and ribs (Figure 12).

Considering this anomaly is an issue of geometry, and previous attempts to minimize warpage via process control were unsuccessful [21], it becomes apparent that physical reinforcement may be one of only a few feasible methods to reduce warpage with these complex geometries.
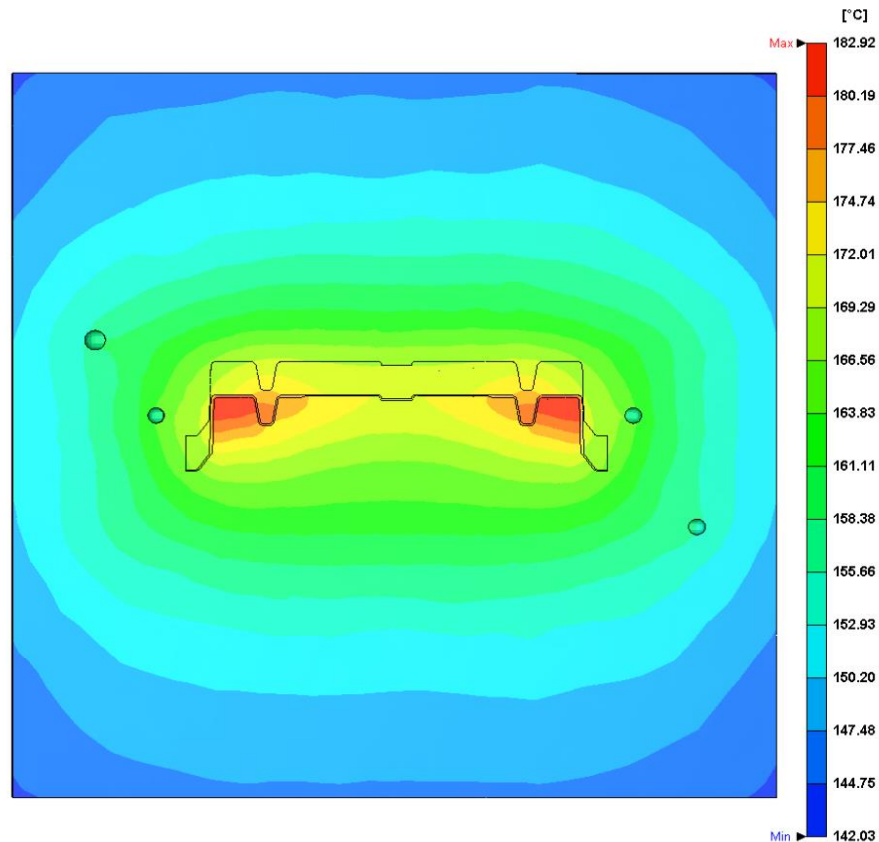
Figure 12: Temperature cross section of mould block, flow cavity (larger part outline), and moulded part (smaller part outline)

Nonetheless, despite the limitations outlined above, thermography remains an excellent tool for parametric studies in which absolute temperature is not as critical as relative temperature. As will be subsequently explored, thermography can be used effectively to understand the effects processing conditions may have on part temperatures and thus warpage, and as a quality control measure to discern deviations from standard operation.

Since thermal behaviour and warpage are so closely connected, examining the warpage pattern between manufactured parts and parts generated from moulding simulation can further support the accuracy of simulation. Seen in Figure 13 is the average warpage pattern of manufactured components from the same processing condition set on top compared to the warpage pattern generated from moulding simulation on the bottom. While not a perfect match, there are similarities between the two. For example, on the seatback outers (left side), the flanges in both patterns warp positively (out of page) and are the source of peak positive warpage, and the centre ribs also deviate outwards with a general bowing behavior occurring longitudinally across the part. The remainder of the part warps negatively into the page with the peak occurring at the base of the part. The seatback inners feature less similarity as the common positive warp on the inner ring 'bleeds' outwards, and the source of peak negative warp is on the flanges in the manufactured parts compared to the base in the simulated part. It is suspected that this is in large part due to the ejection method. The SBIs were found to be ejected in one of two ways: 1) using compressed air delivered from a mould-mounted valve to separate the part from the upper half of the tool, leaving the part sitting in the bottom, or 2) removing the part by force from the upper half. By method 1), the part experiences a brief but strong convective heat transfer, cooling it and influencing the shrinkage and thus warpage. By method 2) external forces are applied to the part, potentially inducing stresses that are relaxed through warpage. Accordingly, warpage of the SBI cannot be reliably predicted with the methods used. In terms of magnitude, the results differ greatly. Similar observations have been found when material properties are separated and micromechanics models are used, with one instance underpredicting warpage by a factor of 4 at times [59]. Other factors can contribute to this discrepancy such as induced stress by the ejection method and post-moulding cooling environment [16].
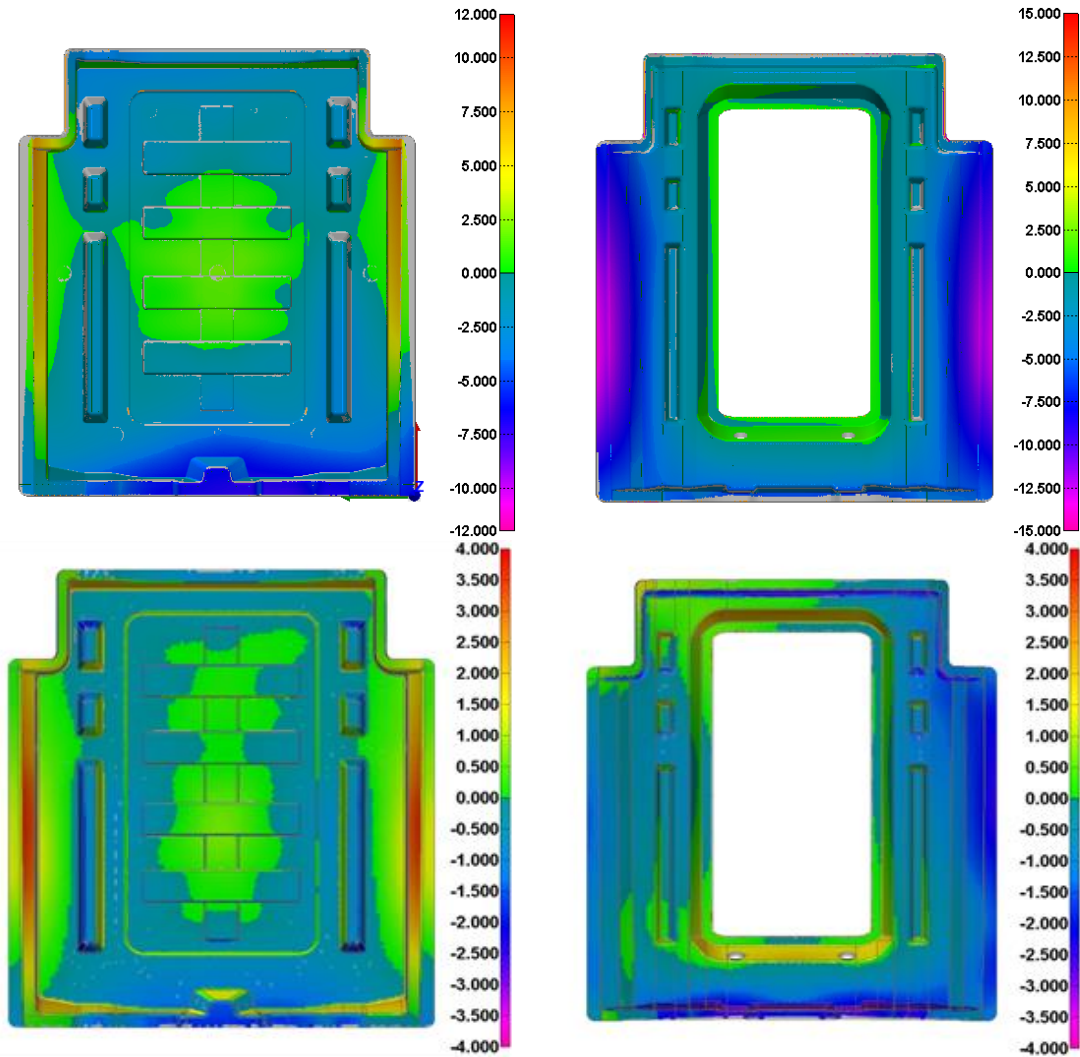
Figure 13: Warpage pattern [mm] of manufactured seatbacks (top) and parts from moulding simulation (bottom)

2.4 Thermography Case Study

2.4.1 Effect of Charge Temperature

Charge temperatures were first analyzed, as the thermomechanical behavior of the material has implications on moulding. Variations in charge temperature and open-air cooling time will change the rate of cooling of the parts, a primary predictor of crystallinity for semi-crystalline polymers and thus shrinkage [7, 8, 60]. Lastly, using charge temperature just prior to mould

closure as a factor may be the most accurate modeling of the process but being a continuous variable might lead to challenges with respect to the upcoming ANOVA model.

To better understand the relationship between charge temperature and LFT-D temperature, LFT-D temperature was used as the predictor variable and the analysis was conducted in Minitab. The p-values for predictors are listed in Table 8 while Figure 14 summarizes these charge temperatures. As expected, the data suggests that LFT-D set point has a strong influence on charge temperature. The observed temperature can vary greatly, with residuals up to 12°C and R2 values of 54% and 72% respectively between trials, most likely due to variable air exposure time caused by the charge being manually transferred between LFT-D and mould. As it was mentioned, this would have consequences on cooling rate, but it is important to remember that this pertains only to the temperature of the charge "skin", in a sense that thermal penetration is likely limited to only 2 to 3 mm on each side of the charge due to the low thermal conductivity of 0.264 W/m-K. Thus, the effect of the aforementioned transferring time may not be significant.

Table 8: Predictor p-values for charge temperature for SBO and SBI

SBO Trial		SBI Trial	
Predictor	**P-Value**	**Predictor**	**P-Value**
LFT-D temperature	0.000	LFT-D temperature	0.000
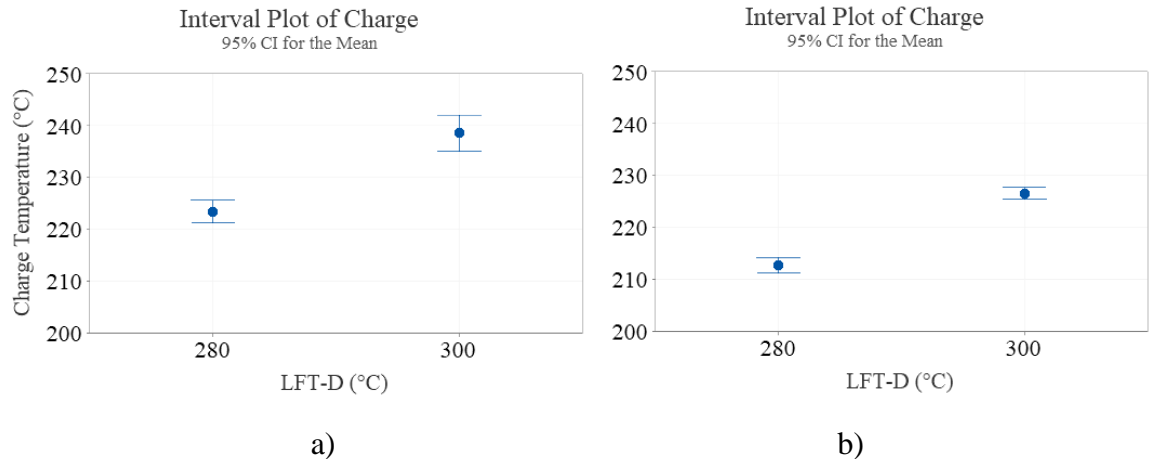
Figure 14: Interval plots of charge temperature groups for: a) SBO and b) SBI (error bars represent one standard deviation)

The results above indicate that LFT-D temperature can be substituted for charge temperature in the statistical model for ejection temperature. When charge temperature was used instead as a covariate in the statistical model for ejection temperature, the variance inflation factors (VIF) indicated an extremely high multi-collinearity that implies correlation or redundancy between factors. Since the LFT-D temperature has a strong influence on charge temperature at the mould-close condition (Figure 14 and Table 8) the aforementioned substitution is recommended. This was reinforced by the fact that when LFT-D set point was used in the statistical model, the VIF reported values indicated minimal to no multi-collinearity.

2.4.2 Effect of Ejection Temperature

When it comes to part configuration, ejection temperatures were investigated both globally and locally. While the global results were useful to understand the general part behavior, local studies could yield results that are otherwise obscured when performing the "lumped" global analysis including all part regions.

2.4.2.1 Global Average Temperature

In this case, the data from the ejected parts was processed through Minitab to determine the influence of process parameters on the part ejection temperatures. The p-values for the ANOVA studies completed for the SBO (R^2 = 78.7%) and SBI (R^2 = 99.8%) are presented it Table 9 (the dependent variable is ejection temperature). The LFT D temperature, hold time, and mould temperature all have a significant effect ($p < 0.05$) even though some small interactions between them are present. Nonetheless, from a practical standpoint, LFT-D temperature, hold time, and interactions all have minimal effects. This is best illustrated by the interval and interactions plots depicted in Figure 15. The scale of the y-axis paired with one standard deviation error bars in Figure 15a suggests that only hold time has an effect on the ejection temperature of SBO, albeit a minimal one. Figure 15b shows very similar groupings between LFT-D temperature levels, thus suggesting that this factor has a minimal effect on SBI ejection temperature. In contrast, hold time shows some effect since ejection temperature decreases slightly when hold time increases. The most prominent effect on eject temperature is that exerted by mould temperature (Figure 15b) even though it was only tested in SBI trials. On the other hand, the parallel lines that are visible in the interaction plots (Figures 15c, 15d) suggest that no interactions between certain pairs of factors are present. Furthermore, even though some of the analyzed lines are not perfectly parallel, the interactions implied by them can be disregarded owed to scaling and measurement errors. Thus, mould temperature has the greatest influence on ejection temperatures, while hold time can influence ejection temperatures only by several degrees at a given mould temperature.

Table 9: Predictor and interaction p-values for eject temperature determined as the global average over the entire part

SBO Trial		SBI Trial	
Predictor or Interaction	**P-Value**	**Predictor or Interaction**	**P-Value**
Orientation	0.175	LFT-D temperature	0.013
Pressure	0.999	Mould temperature	0.000
Hold Time	0.000	Hold time	0.000
Orientation*Pressure	0.047	LFT-D*Mould	0.014
Orientation*Hold Time	0.937	LFT-D*Hold Time	0.016
Pressure*Hold Time	0.745	Mould*Hold Time	0.189
Orientation*Pressure*Hold Time	0.123	LFT-D*Mould*Hold Time	0.003

a)

b)

c)

d)
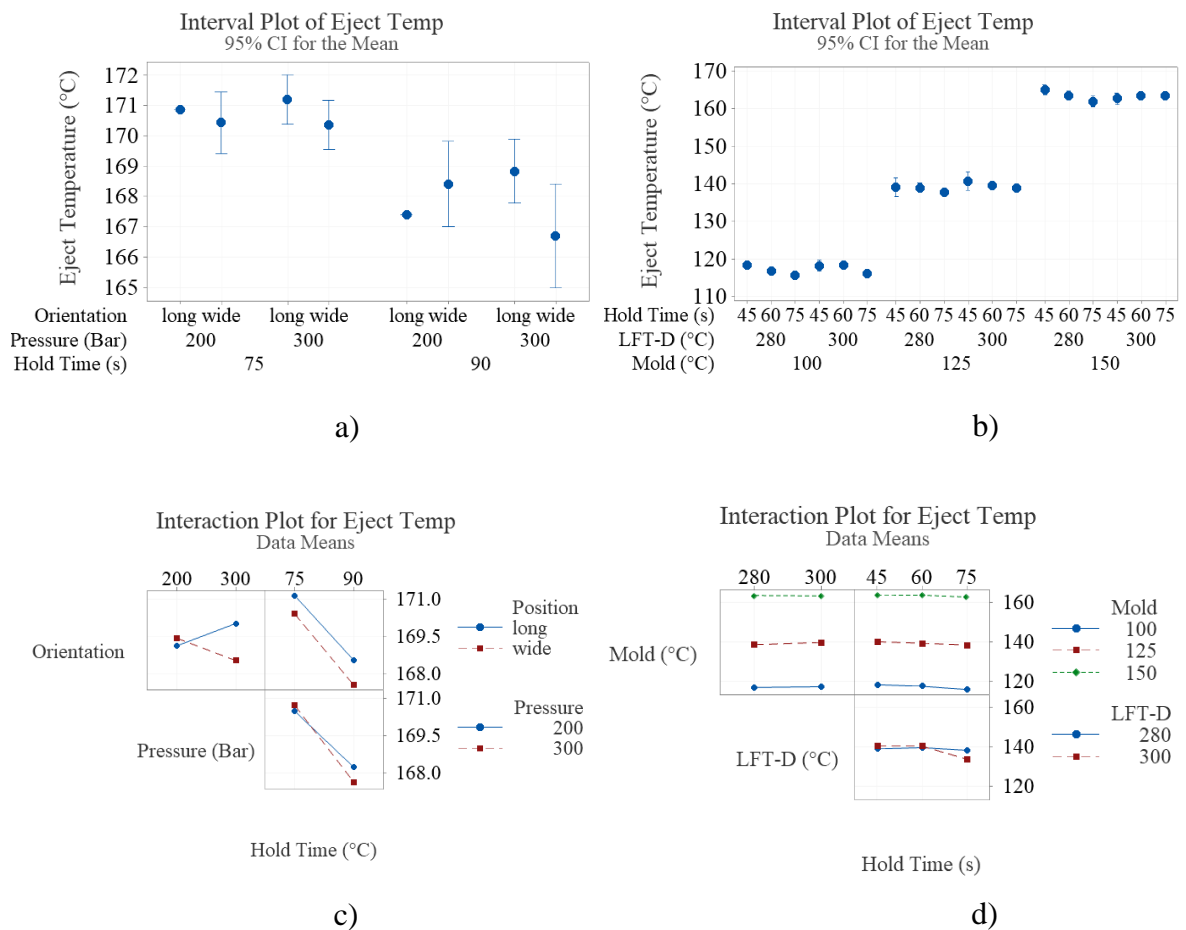
Figure 15: Global average approach – interval plots for: a) SBO, b) SBI and interaction plots for c) SBO, d) SBI (error bars represent one standard deviation)

2.4.2.2 Local Average Temperature

When examining the temperatures of the ejected parts (Figure 7), it became apparent that part

temperatures were non-uniform. Hence, it was deemed of interest investigate parts by focusing

on local, rather than global levels of the temperature. Similar to the entire part, a mask was

applied to the bottom, hotter region (Figure 7c) and data was extracted for each manufactured

SBI. The p-values for this localized study are displayed in Table 10. While several parameters

and interactions exhibit statistical significance ($p < 0.05$), interval and interaction plots

depicted in Figure 16 reveal that most of them do not have practical implications. Nonetheless,

mould temperature continues to have the greatest influence, hold time has a more pronounced

influence, whereas LFT-D temperature has a slight, but noticeable effect. The interactions do

not seem to be important since the lines in Figure 16b are quasi-parallel.

Table 10: Predictor and interaction p-values for eject temperature determined as the local average over the hot region of SBI

Predictor or Interaction	P-Value
Mould temperature	0.000
LFT-D temperature	0.000
Hold time	0.000
Mould*LFT-D	0.000
Mould*Hold time	0.000
LFT-D*Hold time	0.390
Mould*LFT-D*Hold time	0.073
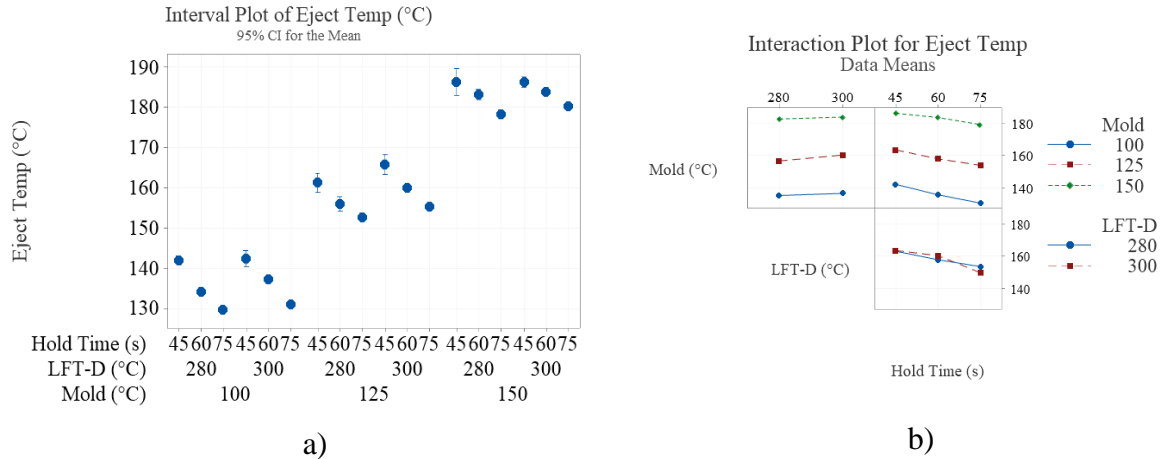
Figure 16: Local average approach for SBI: a) interval and b) interaction plots (error bars represent one standard deviation)

Overall, these results suggest that a certain discrepancy exists between the analyzed global and local approaches in a sense that hold time has a noticeable localized effect. In terms of reasoning for this phenomenon, at least two possibilities can be indicated: i) regional part thickness non-uniformities, and ii) temperature measurement errors caused by environment reflections discussed in detailed in Section 2.3.1. One of the ways to address i) would be to gradually increase hold time in an attempt to reach the steady thermal state across the entire part (including its thicker regions). The homogenization of the temperature to be achieved might also assist with warpage reductions since longer hold times are known to decrease shrinkage [13]. The nonuniformity in part temperature combined with its large local gradients are typically a characteristic of nonuniform cooling rates that in turn lead to variations in crystallinity eventually leading to part warpage.

2.4.3 Significance for Warpage

While warpage represents a common by-product of compression moulding operations, relatively little has been accomplished so far with respect to its accurate measurement [61] and

definition of adequate warpage metrics [37]. According to the general knowledge, polymer composite warpage is seen as the result of relaxation of residual stresses induced in parts from a variety of causes. Perhaps the most significant factor in formation of residual stresses is the cooling rate [11]. In the case of semi-crystalline polymers, higher cooling rates produce lower crystallization temperatures, resulting in more opportunity for residual stresses to be relaxed as once the polymer crystallizes, these stresses become locked into the part [11]. By keeping in mind the distinct eject temperatures groups in Figure 15, it is expected that parts made with higher LFT-D temperature and lower mould temperature would exhibit higher cooling rates and thus markedly less warpage. It is observed that the other factors, namely hold time and pressure do not have such a pronounced effect on eject temperature, however, shorter hold times and lower pressures may not allow for sufficient temperature homogenization and heat conduction respectively, thus affect cooling rate and eject temperature [13].

2.5 Chapter Summary and Conclusions

The main objective of this study was to investigate the causes of warpage within the seatback parts. To achieve this, thermography, physical sensors, and moulding simulation were first correlated and then further analyzed to provide a complete understanding of the observed thermal behaviour. The viability and limitations of thermography in the context of industrial compression moulding were also discussed. Following this, the effect of various process parameters (mould temperature, process pressure) on ejection temperature were also assessed with statistical tools for insight on part warpage. An imaging-based process was developed in order to convert camera readings into an areal temperature profile for the two analyzed parts.

The results suggest that thermography is prone to issues with view angle and reflection causing erroneous apparent temperatures. Certain temperature discrepancies between

simulated and measured data could also be observed and they could be largely attributed to either incorrect camera readings associated with deep features, the use of air ejectors or hot mould components that were located in the vicinity of the surface whose temperature was assessed by means of the IR camera. Beyond this, the experimental results and camera accuracy were compared to moulding simulations and - barring reflections and other external "noise" factors - experimental and simulation results remained comparable. This suggests that the thermographic camera yields accurate temperature readings even at viewing angles that deviate more than 50° from the normal. Furthermore, moulding simulations were found to correspond well to readings from thermocouples and thermographic images where reflections were not likely.

Results from the thermographic data resulting from the experimental moulding trials suggest that mould temperature influences the ejection temperature more than any of the other factors considered in this study. By contrast, hold time has a smaller but noticeable effect, whereas pressure, charge temperature, and orientation do not have an effect within the range of the values tested. This suggests there should be significantly different results in warpage at various mould temperatures and hold times. However, as seen in previous works this is not the case. Paired with the issue of an inhomogeneous thermal state at ejection as a result of the complex geometry, it is likely that a more active solution for warpage must be undertaken if the geometry is to stay the same. Thus, to be explored subsequently is the co-moulding of LFT-D with reinforcing materials with higher fibre content, such as GMT.

Chapter 3 : Co-moulding of GMT and LFT-D

3.1 Overview

Chapter 3 focuses on co-moulding of LFT-D and GMT. Once the warpage had been surveyed it was confirmed that co-moulding may in fact be a suitable robust method for warpage reduction. Prior to this, a method for analyzing assembly of deformed parts was adapted to serve as an appropriate metric for quantifying warpage. Once established, manufacturing trials were conducted, and the warpage was compared between the base materials and co-moulded material. Since the seatback outer and inner share similar features and warpage behaviours, only the seatback outer was chosen for this study as the results would likely see comparable results with the seatback inner.

3.2 Experimental Methods

3.2.1 Materials and Manufacturing

The LFT-D process is illustrated in Figure 1 and described in more detail in sections 1.2.1 and 2.2.1. Again, the LFT-D material used was BASF Ultramid 8202 HS polyamide 6 (PA6) with 40 wt.% Johns Manville glass-fibre. The GMT material format is sourced from Lanxess's Tepex Flowcore family and is also PA 6 but with 60 wt.% glass fibre. It is composed of a randomly oriented chopped fibre mat impregnated with polymer films or melt. The GMT sheets are first heated in an oven to processing temperature then placed on a mould and compressed. In the case of co-moulding, the GMT sheet is placed on the mould first and then the LFT-D charge is placed on top such that the LFT-D flows overtop of the GMT and fills in areas that GMT cannot. This arrangement can be seen in practice in Figure 17, alongside a finished product with the GMT and LFT-D regions distinctly visible. During moulding, it was evident that the GMT material had no issue forming into deep-draw pockets and ribs and the

LFT-D had no issue flowing over top of the GMT and into the far reaches of the geometry. As such, co-moulding satisfies the requirement of high flow lengths and formability for complex geometries.

Figure 17: LFT-D charge laid on top of GMT sheets for moulding in tailored sheet (top left) and rectangular sheet (bottom left) configurations alongside a finished part (right)

Once the cycle completes, the parts must be gently wedged out as the geometry causes the parts to stick to the cavity half until the material shrinks. Since the material is still soft at mould open, the use of ejector pins can destroy the parts as seen in Figure 18, and any excessive forces may induce residual stresses and exacerbate warpage [16]. Use of air ejector valves is also known to alter the thermal state of the parts on one side, a cause of warpage [62]. This brief period of open-air cooling on one half of parts while the other half is still in contact with the heated mould, and the forces required to remove the parts are noted as possible causes of warpage.

Figure 18: Finished part destroyed by ejector pins

The moulding conditions and material configurations can be seen in Table 11. The GMT shapes were chosen based on an ease of manufacturing basis for the plain rectangular sheet and a performance based full-coverage shape for the tailored blank. To determine the optimal reinforcement thickness and shape, the study followed a 2x2 Design of Experiments methodology with statistical processing using Minitab 19 [55, 56]. For analysis, the parts are digitized using a handheld laser line probe scanner per the same methods described in Martin et al [21, 61]. As a comparison to their 'virgin' components, sets of LFT-D and GMT were moulded separately. In each set, 5 replicates were moulded. The set of GMT required 2 layers of 2 mm sheets in order to properly fill the mould and consequentially led to a thickness higher than the nominal average of 3.5 mm, while the base LFT-D and co-moulded sets were at

approximately nominal thickness. This must be kept in mind for results of warpage and material testing as the GMT specimens were 4.35 mm thick.

Table 11: Co-moulding processing and material configuration parameters

Parameter	Level 1	Level 2
Mould Temperature	150 °C	-
LFT Temperature	300 °C	-
GMT Temperature	300 °C	-
Pressure	200 Bar	-
Hold Time	90 s	-
GMT Thickness	1 mm	1.5 mm
GMT Shape	Rectangular	Tailored

3.2.2 Warpage Metrics

3.2.2.1 Deformation Energy Method

Based on the complexity of the parts, it is very possible that inappropriate metrics will conceal important information of the part, i.e., one region or feature suffering from high deformation but the average value still being acceptable as the rest of the part was well within tolerance. Along with this, the SBO is to be joined in an assembly and requires welding in 26 locations as seen in Figure 19, meaning information must be gathered for the entirety of the part and metrics seen in the literature review such as maximum deformation or change of length will not suffice. Thus, a global summative method is preferred.
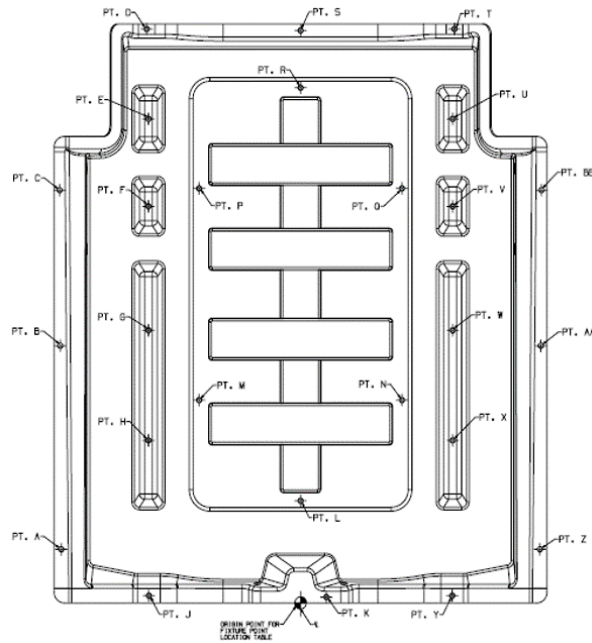
Figure 19: Welding points across the SBO part

Such a global summative method finds its roots from Martin [21] and Maia [52], wherein the scanned part is aligned to the nominal geometry via the centre section ribs as this is deemed to be the stiffest section and least prone to warp. Thus, the point of zero warp is also located within this region. Then, the deviation from nominal of approximately 2000 probes are applied as displacement boundary conditions for a structural analysis of the nominal part in Abaqus. The mesh used for this structural study utilized C3D10M tetrahedral elements with a mesh size of 4 mm. This process mimics the change in shape of the parts and allows for that change to be measured using total strain energy, however, a dummy material will be used for all material configurations such that the deformation energy is purely a geometric measure for comparative purposes. This method may also reveal some information relating to the sensitivity of warp for each deformation mode as it will account for differences in local geometric stiffnesses. The total strain energy in Abaqus is represented by the following equation [63]:

$$ALLIE = ALLSE + ALLPD + ALLCD + ALLAE + ALLQB + ALLEE + ALLDMD \quad (17)$$

where ALLSE is the recoverable strain, ALLPD is energy dissipated through plastic deformation, ALLCD is energy dissipated through creep, swelling, and viscoelasticity, ALLAE is artificial strain energy used to remove singular modes, ALLQB is energy dissipated through infinite elements (unused), ALLEE is electrostatic energy (unused), and ALLDMD is energy dissipated though damage (unused). The relevant equations are listed as follows, integrated over volume and time [64]:

$$ALLSE = \int_0^t (\int_V (\frac{1-d_t}{1-d}) \boldsymbol{\sigma}^{\ c} : \dot{\boldsymbol{\varepsilon}}^{el} dV) d\tau \quad (18)$$

$$ALLPD = \int_0^t (\boldsymbol{\sigma}^c : \dot{\boldsymbol{\varepsilon}}^{pl} dV) d\tau \quad (19)$$

$$ALLCD = \int_0^t (\boldsymbol{\sigma}^c : \dot{\boldsymbol{\varepsilon}}^{cr} dV) d\tau \quad (20)$$

where d and d_t are the damage parameter and the damage parameter at time t respectively, $\boldsymbol{\sigma}^c$ is the Cauchy stress tensor, and $\dot{\boldsymbol{\varepsilon}}^{el}$, $\dot{\boldsymbol{\varepsilon}}^{pl}$, and $\dot{\boldsymbol{\varepsilon}}^{cr}$ are elastic, plastic and creep strain rates respectively.

One caveat to this method is the reliance in reverse engineering software – PolyWorks in this case – to match probe points from the nominal CAD to the scanned deformed geometry. While this works well for displacements along the normal axis, the software cannot guarantee a perfect match if the displacement is off axis from the normal since it searches for the closest point [65]. At times, the software cannot find a corresponding point at all and thus the deformation at that point cannot be specified. Manual mapping has been explored to solve this in Martin et al [37], but would not be practical for thousands of points.

3.2.2.2 Structural Similarity Index Measure

In general, it is useful to be able to measure the possible alteration of warp pattern because of co-moulding with a reinforcement, but it is also beneficial to be able to recognize and quantify this change in case co-moulding affects assembly or performance further along the line. As a result, an image correlation metric can be used, such as the Structural Similarity Index Measure (SSIM), to compare warp patterns between material configurations [66]. This metric aims to resolve human perception into three 3 key parameters, luminance, contrast, and structure in the following general form:

$$SSIM(\mathbf{x}, \mathbf{y}) = [l(\mathbf{x}, \mathbf{y}))]^{\alpha} \cdot [c(\mathbf{x}, \mathbf{y})]^{\beta} \cdot [s(\mathbf{x}, \mathbf{y})]^{\gamma} \tag{21}$$

where $\mathbf{x}$ and $\mathbf{y}$ are the two image signals being compared, l, c, and s, are functions of the mean signal intensity of luminance, standard deviations of each signal for contrast, and image structure respectively, and α, β, and γ are adjustable based on the relative importance of each function [66].

MATLAB offers a function that applies this algorithm to two imported images. The images selected are of the front face of the parts with their respective warpages resolved into positive and negative magnitudes as black and white since only the pattern is of concern and not magnitude. Such an example of images to be compared can be seen in Figure 20. The warpages of each set of parts will be averaged within PolyWorks and will be compared to the reference set of LFT-D and GMT material for insight into pattern variations.

Figure 20: A sample of two warpage patterns to be compared via SSIM

3.3. Warpage Results

3.3.1 Deformation Energy Results

The result of the manufacturing trials in terms of deformation energy are summarized in Figure 21. at first glance it is interesting to note that the warpage magnitude associated with co-moulding LFT D and GMT can be very similar to that of the nominal parts made with only the reinforcing material, GMT. In this case, replacing approximately just 25% of the LFT-D volume with GMT in the tailored blank configuration can lead to warp magnitudes very close to the nominal GMT parts. It would also seem as though increasing the GMT content has a negative effect on warpage and is supported by an ANOVA model seen in Figure 22 and Table 12. The low R-squared values but significant p values ($p < 0.05$) indicate that the model does not represent the data particularly well but that the material configurations are appreciably different from one another.
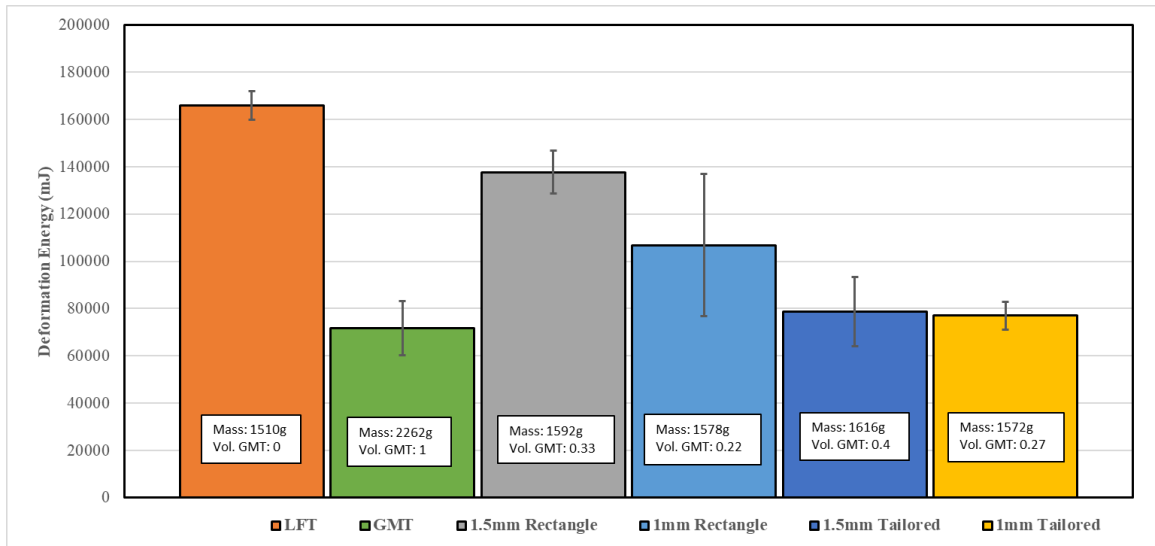
Figure 21: Summarized co-moulding warpage results for deformation energy metric
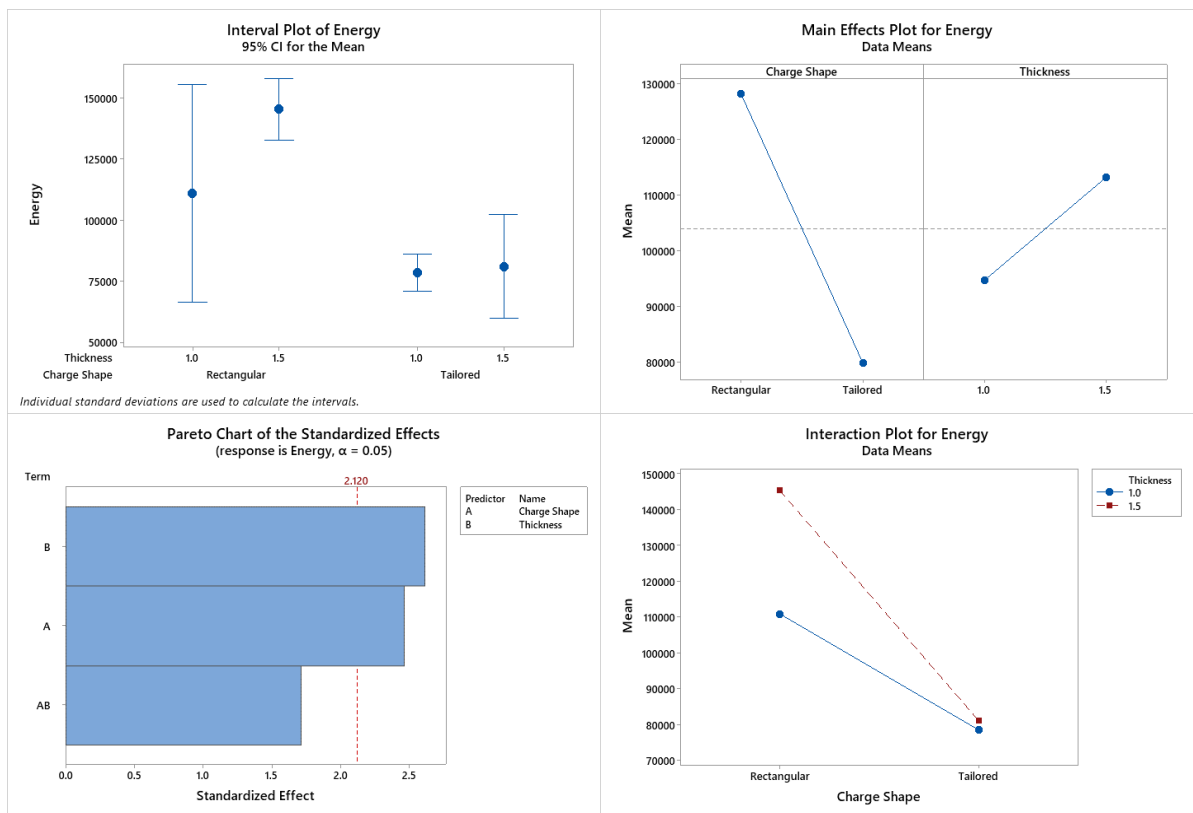
Figure 22: Plotted ANOVA modelling results for co-moulding trial

This modelling divergence stems from the higher variance in warpage in some of the sets, possibly due to placement, forming, or cooling inconsistencies during and post-manufacturing, or perhaps a physical interaction between the LFT-D and GMT.

Table 12: Tabulated results of the ANOVA modelling

Analysis of Variance		Model Summary			
Source	**P-Value**	**S**	**R-sq**	**R-sq (adj)**	**R-sq (pred)**
Charge Shape	0.025	20773.4	67.90%	61.88%	49.84%
Thickness	0.019				
Charge Shape*Thickness	0.107				

Contour plots of part warp can be seen in Figure 23 and reveal more information about the warp behavior. The sets which used the rectangular cut GMT sheet resulted in much more pronounced bowing across the longitudinal direction of the parts, comparable to the base LFT-D sets. Perhaps difficult to confirm without further simulation or testing, but this may be a result of the change in thickness of LFT-D near the center of the part along the longitudinal direction as seen in Figure 17, causing residual stress concentrations from thermal shrinkage or reduced load transfer efficiency when ejecting parts from the mould. These stress concentrations may also be exacerbated by how well the materials are bonded to one another, which could be seen in a morphological analysis. Further, the magnitude of change in LFT-D thickness may have a role as well, i.e., how near the morphology is to a pure discontinuity of material or a butt joint. This could explain why the rectangular sets suffer much more than the tailored sets when the GMT thickness increases as the stress concentration occurs in the center rather than near the edges of the part in the case of the tailored sets.
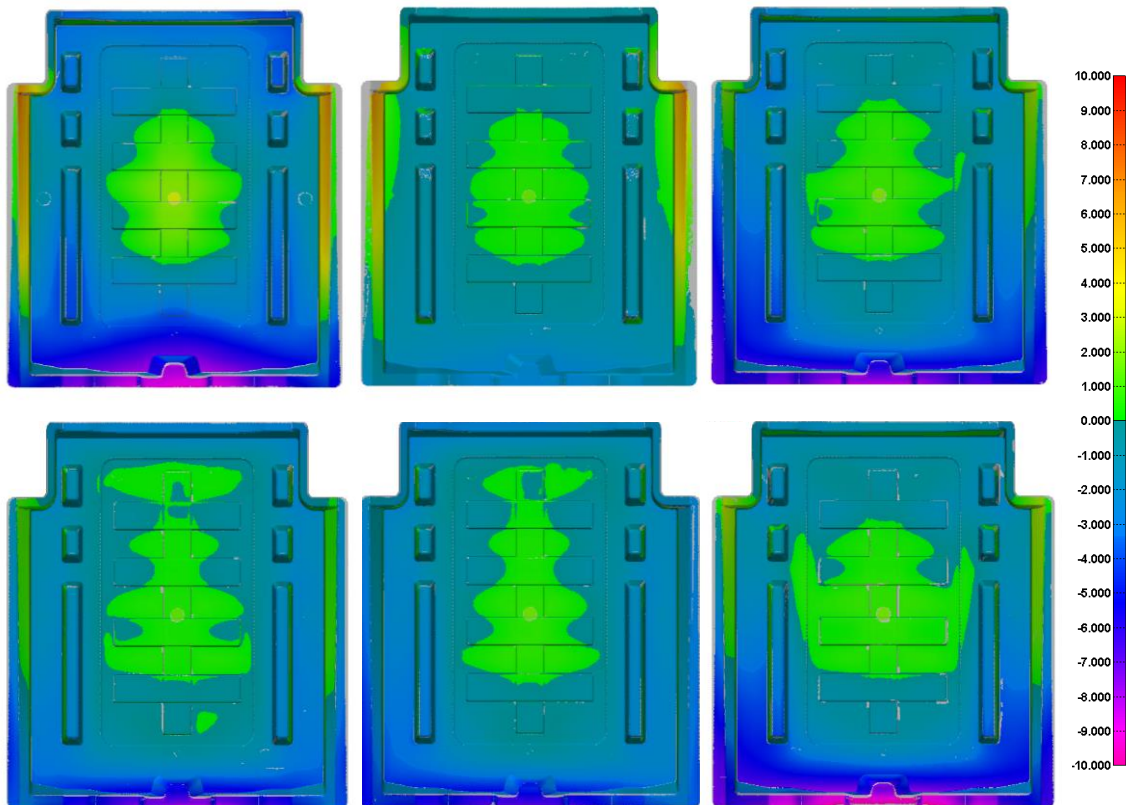
Figure 23: Warp contour plots (clockwise from top-left: LFT-D, GMT, 1 mm rectangle GMT, 1.5 mm rectangle GMT, 1 mm tailored GMT, 1.5 mm tailored GMT)

3.3.2 SSIM Results

The summarized results of the SSIM metric can be seen in Table 13. To contextualize these values, Table 14 has been provided as well. Table 14 originates from measurements taken from LFT-D parts produced within Martin et al [37], moulding simulation from Chapter 2 and Knezevic et al [62], and the influence of blank corners in Figure 20 which cannot be cropped from the analysis. It is apparent that the warp pattern does not deviate significantly from the reference sets of pure LFT-D and GMT, albeit a stronger similarity is seen to LFT-D. In other words, with Table 14 in mind, the co-moulded parts could be seen as replicates within the same set as the original pure LFT-D. In general, as seen in Figure 20, the warp pattern for all sets is

in the positive direction (out of page) in the center and along the upper lengths of the lateral flanges and negative (into the page) everywhere else. Some information is hidden by this angle, such as the spring-in of the side walls, however the direction of warp on the flanges is most often indicative of the direction of warp (positive or negative) along their adjacent side wall.

Table 13: Warp pattern SSIM results

Reference	Test	SSIM (0-1)
LFT	GMT	0.8253
LFT	1.5 mm Rectangular	0.8198
LFT	1 mm Rectangular	0.8423
LFT	1.5 mm Tailored	0.8068
LFT	1 mm Tailored	0.8086
GMT	1.5 mm Rectangular	0.7535
GMT	1 mm Rectangular	0.7777
GMT	1.5 mm Tailored	0.7604
GMT	1 mm Tailored	0.7653

Table 14: Contextual values for SSIM interpretation

Contextual Category	SSIM
Most similar parts (within same set)	~0.9
Most different parts (within same set)	~0.8
Simulation vs experiment	~0.5-0.6
Background influence	~0.05

What these results represent for practical applications is that manufacturers may not have to dwell on changes in part behavior due to GMT co-moulding. This is most consequential for design processes where co-moulding was opted for after initial moulding results were gathered. These projects may have already relied on a certain behavior for part fit-up and assembly and mitigating required changes should be prioritized. An example of this can occur during new vehicle launches, wherein manufacturers ensure good fit-up by modifying tolerance bands and tooling for assembly and other parts. If the warp pattern remains consistent

after the switch to co-moulding, the hassle of remodifying the process and recertifying parts is lessened.

3.5 Chapter Summary and Conclusions

In this chapter, an experiment was conducted to learn if co-moulding of LFT-D and GMT was possible and if the resulting product featured reduced warpage compared to base LFT-D. With this, two metrics were adapted to examine the magnitude of warpage and to compare the pattern of warpage between different material combinations.

Through this study of co-moulding LFT-D materials with GMT, several key points have been addressed for automotive manufacturers in their quest in vehicle lightweighting. First, co-moulding of LFT-D and GMT maintains the desirable high flow lengths of LFT-D required for complex geometries; part warp is greatly reduced, comparable to parts made purely of the higher fibre content GMT; the required volume displacement has been shown to be approximately only one quarter; and lastly, the change in warp behavior is insignificant.

All the aforementioned issues indicate co-moulding is a robust and effective method for reducing part warp in mass-manufactured complex geometries. However, some open items remain and must be investigated to verify its potential. Included in this is mechanical testing of specimens for comparison to pure LFT-D and GMT samples to examine use-case performance and morphology analysis to determine the extent of bonding between the materials.

Chapter 4 : Material Testing of Co-moulded Parts

4.1 Overview

Chapter 4 provides further detail about the feasibility of co-moulding the same constituent materials in different formats. Here, the mechanical properties are tested to confirm that the materials are properly bonded and perform as expected. Optical microscopy is also used on several specimens to search for possible anomalies at the interface of the materials.

4.2 Mechanical Testing

4.2.1 Testing Methods

Three tests were chosen to examine the performance and bonding of the materials. Namely, tensile testing to characterize tensile strength and elastic modulus, three point bending flexural testing to mimic in-car functionality, and short beam shear (SBS) testing to examine interlaminar shear strength between the two layers of material. The corresponding standards followed were ASTM D638 – 14, ASTM D 790 – 17, and ASTM D 2344 respectively. The locations specimens were sourced from on the seatback outers can be seen in Figure 24 with their respective dimensions listed in Table 15. Considering LFT-D charge placement was longitudinally in the centre of the mould, the test locations will be primarily crossflow, meaning the LFT-D fibres will be in the latitudinal direction of the specimens. While not ideal and underrepresenting material properties, the ribs and changes in thickness greatly limited sampling locations. For each test and material there were 8 samples originating from 2 locations in 4 parts each from a set of GMT, LFT, and the 1 mm tailored GMT co-moulded set as this was the best for warpage performance. While again this is not enough for a full characterization, it is enough data points for an initial approximation of the performance and bonding.

Figure 24: Mechanical testing sampling locations (top: short beam shear; middle: tensile; bottom: flexural)

Table 15: Mechanical testing specimen dimensions (* short beam shear only performed on co-moulded set; ** only gage dimensions given)

Material	Dimension (mm)	SBS *	Flexural	Tensile**
LFT & Co-moulded	Width	7	14	13
	Length	21	68.8	57
	Thickness	3.5	3.5	3.5
GMT	Width	-	17.4	13
	Length	-	69.6	57
	Thickness	-	4.35	4.35

First, the sampling sites were marked out and the areas surrounding the samples were rough cut with a band saw. Following this, the actual specimens were extracted using a water jet cutter. Then, prior to testing the specimen were dried for 24 hours to ensure the nylon did not retain any moisture which could skew test data. The test machine used for all three tests at

the Fraunhofer Project Centre was an MTS Criterion Model 45 electromechanical universal test system and images taken of the fixturing setup for each test can be seen in Figure 25. In the case of tensile testing, strain was measured using a Imetrum IM-LENS-MT010 video extensometer.
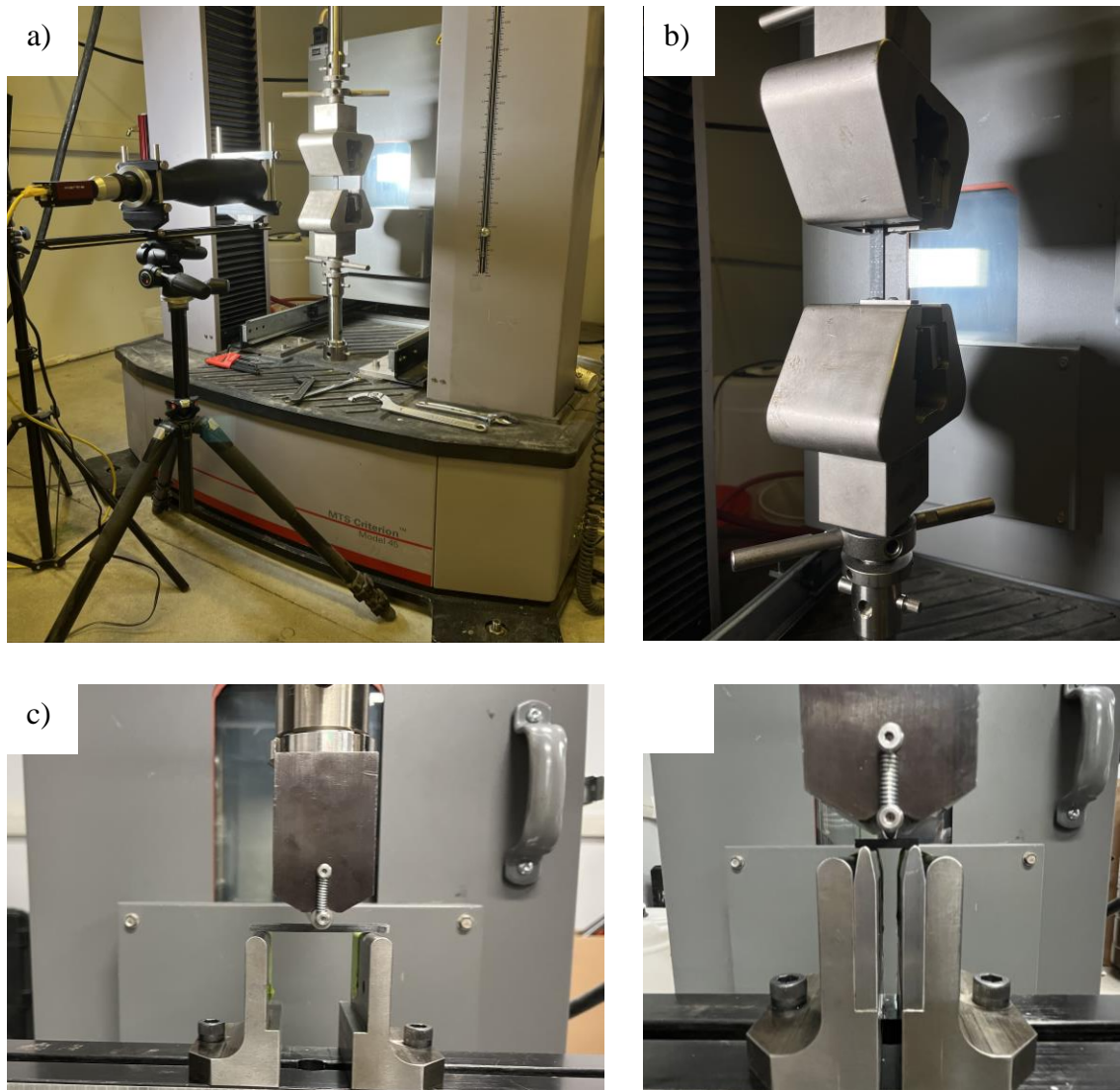
Figure 25:Mechanical test setups including a) tensile including extensometer, b) tensile fixture, c) 3-point bending flexural fixture, and d) short beam shear fixture

Since the co-moulded material is technically a laminate with 2 plies of varying properties, material data for bending properties is not computed so easily. To circumvent this

issue, the specimen is assumed to be composite beam and as such, the transformed section method can be used to find the location of the neutral axis and thus stress in each ply [67]. This method functions by transforming the cross section of one ply into an equivalent cross section of the other by a factor, n, given by:

$$n = \frac{E_2}{E_1} \tag{22}$$

where E_1 and E_2 are the elastic moduli of each material. Then, the neutral axis can be found via the following:

$$\bar{y} = \frac{A_1 \bar{y_1} + nA_2 \bar{y_2}}{A_1 + nA_2} \tag{23}$$

where A_1 and A_2 are the respective cross-sectional areas, and $\bar{y_1}$ and $\bar{y_2}$ are the distances from a reference face to the centroid of each ply. With the neutral plane known, the peak stress in each component can be modelled using the following two equations:

$$\sigma_{x1} = -\frac{My}{I_t} \tag{24}$$

and

$$\sigma_{x2} = -\frac{nMy}{I_t} \tag{25}$$

Where y is the distance from the neutral axis, M is the bending moment approximated as a simply loaded beam with a central load described as:

$$M_{L/2} = \frac{PL}{4} \tag{26}$$

where P is the peak load, and L is the specimen span. I_t is the combined area moment of inertia for each ply given by:

$$I_t = I_1 + nI_2 \tag{27}$$

With this in hand, the strengths of the co-moulded materials can now be found.

4.2.2 Test Results and Discussion

The mechanical testing data has been summarized in Table 16. Intuitively, one would expect the results for strength and modulus of the co-moulded set to lie in between the properties of GMT and LFT, similar to the observed warpage. While this is true in the case of tensile modulus and flexural strength, it appears that in the case of tensile ultimate strength and bending modulus, the properties are lower than in base LFT.

Table 16: Summarized results of mechanical testing

Test	Material	Ultimate Strength (MPa)	Standard Deviation (MPa)	Modulus (MPa)	Standard Deviation (MPa)
Tensile	Co-moulded	49.4	27.1	9969	1562
	GMT	169.2	23.8	14230	1258
	LFT	55.3	4.9	4409	395
Flexural	Co-moulded	262.5	84.4	7063	1519
	GMT	369.9	16.9	17520	2533
	LFT	215.4	26.7	9616	1284
SBS	Co-moulded	19.3	7.2	-	-

However, there are reasonable explanations for these phenomena. The first and most obvious rationale is that the materials are poorly bonded, whether due to air gaps or weld lines caused by moulding underneath the melt temperature of the material. While this may be true for some cases, given the larger standard deviations of the co-moulded material, the short beam

shear testing likely disqualifies this hypothesis. Seen in Figure 26 are the SBS test specimens which appear to fail in flexural tension in the GMT layer before any delamination occurs with only one sample exhibiting noticeable delamination between the LFT and GMT. The top two samples were tested until complete failure to highlight the damage evolution which again follows a crack propagation from tensile failure. Considering these results, there are other, more likely reasons for the strange results.

Figure 26:Post-fracturing short beam shear specimens

The other explanation should have been expected prior to testing. Once the specimens are cut from the seatbacks into flat plates with the band saw, the residual stresses within the workpieces are no longer constrained by the surrounding geometry and are free to deform the piece since it has a lower area moment of inertia. In each case, the pieces curl around the LFT

side as it features a lower modulus than the GMT. They deform further – albeit a smaller amount due to the similar area moment of inertia – when cut with the water jet. Scans of a specimen were taken at each stage, from in-part to post-band saw to post-water jet to examine this evolution. Shown in Figure 27 is the top side of a prepared tensile specimen, of 3.5 mm thickness, with a peak deflection of approximately 5 mm. Thus, when the specimens are placed in the jaws of the tensile fixture, a pre-load stress is introduced to straighten them, producing a stress concentration in the grip sections where contact is made.
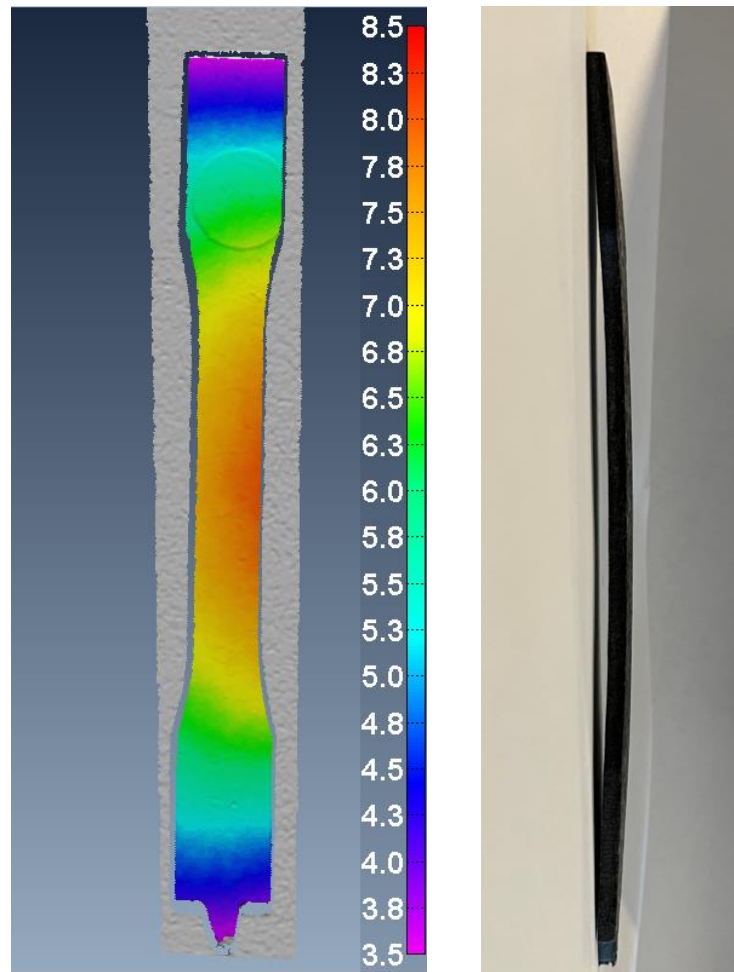
Figure 27:Deviation of work pieces post-water jet out of plane (left) and sideview of deflected specimen (right)

Additionally, failure of the co-moulded specimens, seen in Figure 28, occurs a majority of the time within the grip sections or fillet radii, beginning in the LFT ply and propagating from there, a problem not seen with the LFT or GMT pieces.
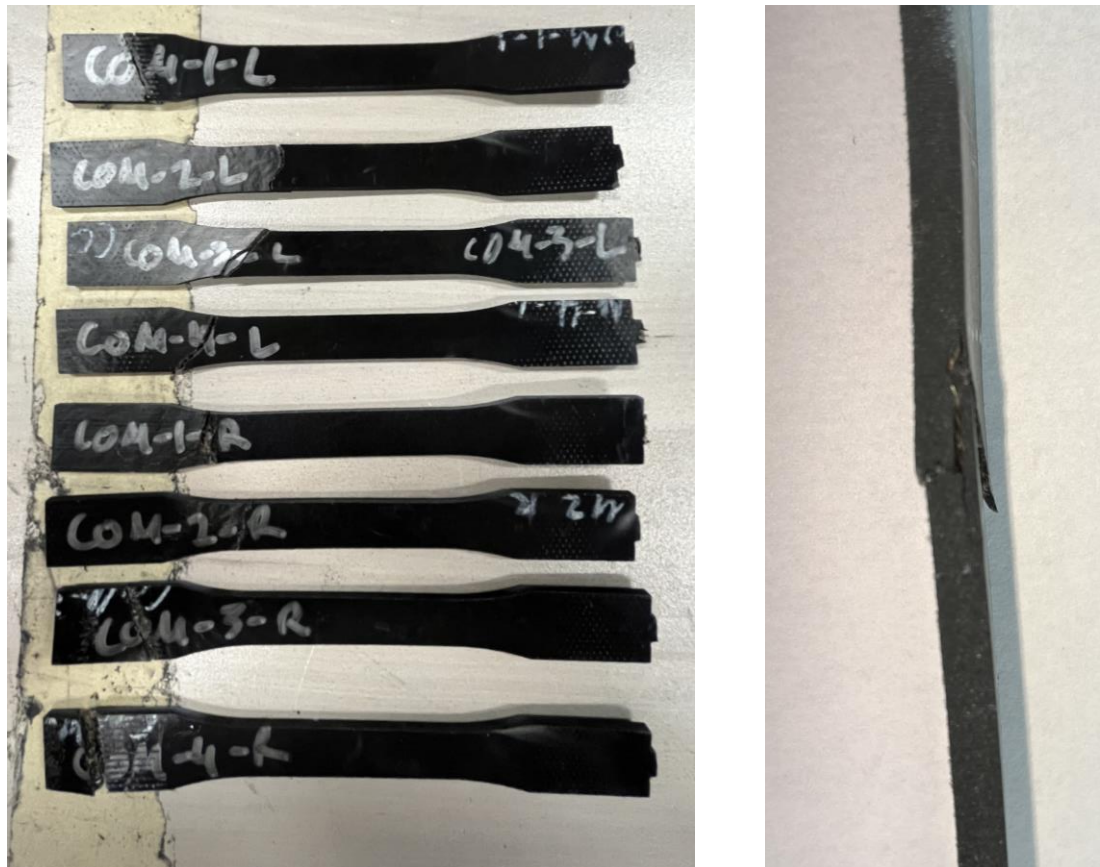
Figure 28: Fractured co-moulded specimens showing fracture in grip sections (left) and sideview of fractured specimen (right)

To further prove this hypothesis, the tensile pre-load applied to the specimens can be approximated, added to the tensile stress experienced during testing, and then compared to the theoretical strength. The radius of curvature of the scanned post-water jet cut specimens was measured in CAD and due to the near exact circular nature of the curvature, the specimens are

approximated using Euler-Bernoulli beam theory [68]. As such, the strain at a point of the cross-section is given as:

$$\varepsilon_x = \frac{dx' - dx}{dx} = -\frac{z}{\rho} \qquad (28)$$

where dx and dx' are the lengths of an infinitesimal element on the neutral axis before and after bending, z is some distance from the neutral axis and ρ is the radius of curvature. The axial stress in a given ply's cross-section can then be found using Hooke's law, where n denotes the ply:

$$\sigma_{nx} = E_n \varepsilon_{nx} \qquad (29)$$

Doing this for a specimen with a 6 mm deflection yielded a stress of 14.4 MPa, which when added to the test result average of 49.4 MPa, yields an approximate total tensile strength of 63.8 MPa for the co-moulded specimens. While considerably more complex in reality, a simple rule of mixtures weighted mean is used as a basic estimate for the tensile strength:

$$\sigma_T = f\sigma_1 + (1-f)\sigma_2 \qquad (30)$$

where f is the volume fraction of LFT-D, and σ_1 and σ_2 are the observed tensile strengths of LFT and GMT respectively. This yields an estimated theoretical strength of 84.9 MPa, some ways off from the off from 63.8 MPa. However, three outlier samples fractured below 23 MPa, and when removed, the average observed test strength is 68.4 MPa, yielding an approximate tensile strength of 82.8 MPa, now close to the theoretical value. As previously mentioned, these outliers may have had bonding issues from moulding or delamination resulting from residual stress release. In either case, proper characterization of these types of materials can be difficult and results obtained exclusively from mechanical testing may not fully represent the

actual material properties. After further examination, the materials perform nearly as expected

and the bonding between them can be good if proper care is taken, barring some outliers.

4.3 Optical Microscopy

To further explore the bonding of the materials, the interface between them is examined. There

are several key defects or anomalies that are sought out to determine how well materials have

bonded: including weld lines, a common defect in injection moulding of plastics which occur

when two polymer flow fronts meet, causing structural weakness [69-71]; air gaps and voids,

which can occur if air cannot vent after the LFT charge is placed on the GMT sheet or if it

becomes trapped underneath the LFT flow front; and fibre discontinuity across the interface,

which may diminish the interlaminar shear strength. Ideally, one would hope for diffusion of

polymer chains between the materials, ensuring the best bond possible, however this occurs on

the time scale of hours to days even [72, 73], such that only surface bonding can be hoped for.

4.3.1 Method

Given that these defects were able to be detected quite well in literature using microscopy [26,

70, 71], this imaging technique was selected. The procedure was completed for three samples

of 1 mm, 1.5 mm, and 2 mm GMT sheet thickness. The samples were water jet cut, mounted

in epoxy, and rotary polished using pads ranging from 200 to 1500 grit before being placed

under a Keyence VHX-6000 digital microscope at Surface Science Western in London,

Ontario. Images were taken at 300x with glare reduction and auto-white balancing.

4.3.2 Imaging Results

A section of a sample micrograph is displayed in Figure 29 as the full images are too wide to

present meaningfully in this format. There is a clear distinction between the two plies, with the

GMT layer having a considerably higher concentration of fibres in the lower section compared to the LFT above it. The GMT also features a much higher isotropic orientation of the fibres that are seemingly stacked in layers, likely arising from the layering process of glass fibre mats. The orientation of the LFT fibres is mostly through the plane of the page as this cross section was taken across the flow direction of the charge. As such, one can immediately understand how co-moulding improves warpage characteristics of LFT-D, both through increased fibre concentration and isotropy.
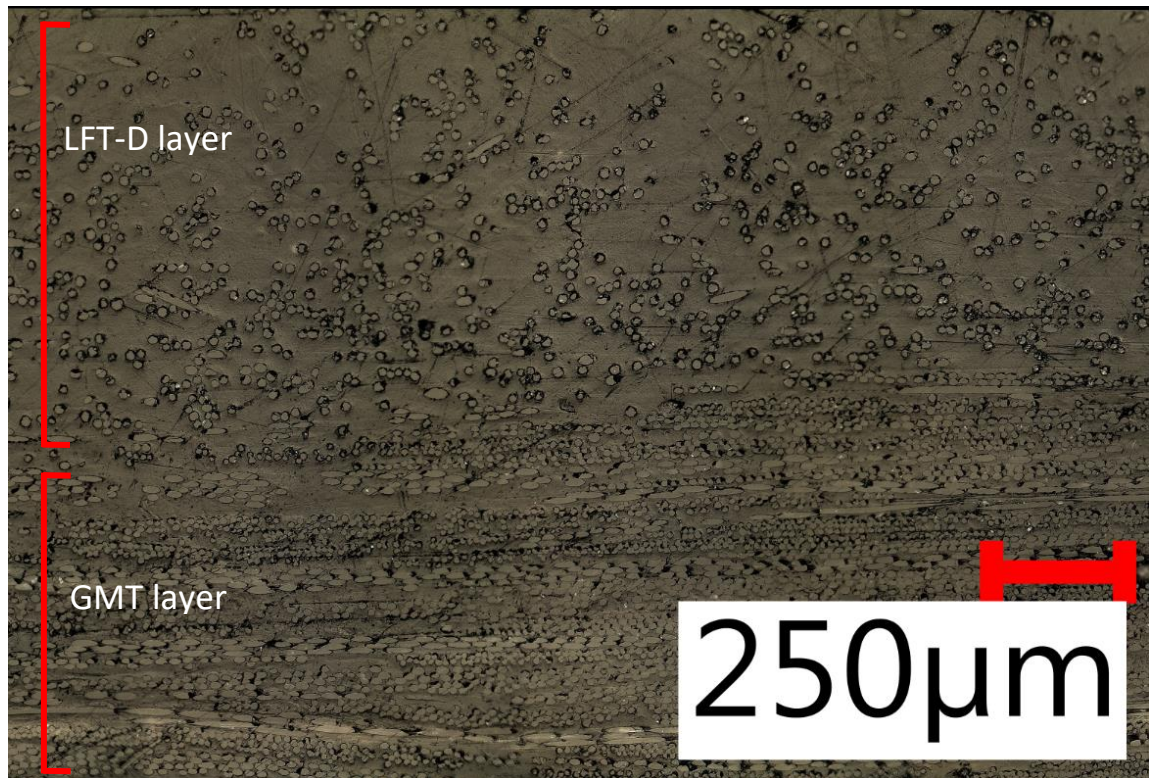
Figure 29: Micrograph section of 1 mm GMT co-moulded sample

Looking closer at the interface, there are no weld lines in any of the samples or any other discernable separators between the plies other than the change in fibre concentration. This is optimal as it means the nylon 6 in each material has successfully fusion bonded and the polymer chains have diffused and entangled between the plies [26]. There is also a lack of any

voids or air gaps between the plies meaning that air was able to vent during flow, and the shear stresses created by the LFT flow did not create voids at the interface. Though, there appears to be notable small voids – denoted by the black spots adjacent to fibres – deeper within the GMT layer, but these may simply be a common side effect of GMT moulding and show little to no effect on structural integrity [26, 74]. Lastly, when examining entire images, the GMT layer is not perfectly straight and is more akin to a wavy profile and in some sections, it is nearly impossible to tell where the GMT ply ends where the LFT begins in terms of fibre concentration. This phenomenon is again likely accredited to the shear stresses created by LFT flow, causing physical deformation of the GMT and diffusion of fibres across the interface [26]. These criteria all point to good bonding between the materials; however, this is only for 3 specimens on the scale of millimetres within 1 location and it is without a doubt an inconclusive study considering the effects geometric features or even radial distance may have on fusion bonding, voids, and fibre discontinuity. Considering some of the mechanical test data suggests inconsistent bonding, it may be a more fruitful venture to mechanically test various locations of the parts to identify problem areas for future microscopy rather than sampling the entire part.

4.8 Chapter Summary and Conclusions

In this chapter, specimens were extracted from the parts co-moulded in Chapter 3 for the purpose of mechanical testing and imaging. Tensile, flexural, and interlaminar shear tests were conducted to approximate the performance of the material in terms of properties and bonding. Microscopic imaging was conducted to further review the bonding and interface between the materials.

Based on the testing done it can be said that the co-moulding should also improve mechanical properties on top of warpage. That being said, the data is somewhat inconsistent, possibly on two accounts: inconsistent bonding and inherent specimen curvature. Microscopic imaging yielded good results in terms of fusion bonding, lack of gaps and voids, and fibre diffusion at the interface. Again, this sample size was not enough to form a consensus but was indicative that future work should yield results that show the performance of the material lies in-between LFT-D and GMT and that the materials are sufficiently bonded.

Chapter 5 : Conclusion and Future Work

5.1 Conclusions

Owed to the quick cycle time, high flow lengths, possibility for large complex components, and the customizable, turnkey nature, the LFT-D process remains attractive to automotive manufacturers. Along these lines, the current thesis has shown promising abilities to reinforce LFT-D materials with GMT in order to reduce the high warpage found in the mentioned geometries.

Using thermography, physical sensors, and moulding simulation, it was found that alongside the common warpage sources of anisotropy and thermal shrinkage, the complex geometry of the parts has trapped heat and this led to inhomogeneous cooling. Thus, without modifying the geometry or mould, and based on previous unsuccessful attempts at modifying processing conditions, co-moulding LFT-D with a reinforcement such as GMT was one of the options to be explored as a possible warpage reduction avenue.

Overall, the co-moulding the LFT-D charge on top of the GMT sheets proved to be a relatively feasible option for warpage reduction. The LFT-D material was able to flow overtop of the GMT and fill in the locations where the low-flow length GMT could not on its own. More specifically, GMT was proven to reduce the warpage found in LFT-D with approximately only 25% volume replacement and provided nearly the same magnitude of warpage found in the GMT-only parts. Even though these results may vary for different part geometries, they are capable of laying out the foundation for future work in this direction.

Mechanical testing of these specimens yielded some inconsistent results, primarily owed to specimen bowing from residual stress release during cutting and possible poor bonding in some instances. However, when outliers were removed, the observed results when accounting for pre-loading were nearly as expected. Further exploration of cross-sections using

microscopy presented results that indicated bonding was quite good, with no sign of structural anomalies. While these tests were of a small sample size, they again set the basis for future work. Based on all these results, it can be concluded that co-moulding of LFT-D with GMT to reduce warpage is a valid and feasible method for warpage reduction and should ultimately prevent fracture during joining of composite assemblies by limiting the amount of force required.

5.2 Future Work

Even though the results captured in this thesis are promising, there are several outstanding issues prior to this strategy being reliably deployed to industry. Firstly, moulding simulations of LFT-D and GMT have to be completed for a variety of reasons. It is also anticipated that such simulations would include a routine that allows the extension of the simulations to other geometries, but they will also enable the monitoring of trapped air, fibre orientation, residual stresses and ultimately comparisons with respect to physically measured warpage. Though, a custom code may be required to simultaneously simulate the draping of GMT with LFT-D flowing overtop, and as such, this work can be used as a calibration tool.

In addition to this, further mechanical testing will also need to be conducted to fully understand the properties and bonding of the co-moulded material. Microscopy should also be conducted at the fracture surfaces to provide additional insights about the interface and damage evolution of the materials. Further to this, a DoE should be conducted in order to find the best processing conditions for bonding. The deformation warpage metric could also be modified to yield energy per unit volume in order to compare results between geoemtries as well. Last but not least, the results outlined here will have to be compared to more traditional reinforcement methods such as the use of continuous unidirectional fiber tapes. It is possible that these

methods would yield better results, but they will also require much more careful approaches in design and manufacturing.

References

1. Ibeh, C.C., *Thermoplastic materials: properties, manufacturing methods, and applications*. 2011: CRC Press.
2. Vaidya, U. and K. Chawla, *Processing of fibre reinforced thermoplastic composites.* International Materials Reviews, 2008. **53**(4): p. 185-218.
3. Krause, W., et al., *LFT-D—a process technology for large scale production of fiber reinforced thermoplastic components.* Journal of Thermoplastic Composite Materials, 2003. **16**(4): p. 289-302.
4. McLeod, M., et al. *Morphological and mechanical comparision of injection and compression moulding in-line compounding of direct long fibre thermoplastics*. in *10th Annual SPE Automotive Composites Conference and Exhibition*. September 15, 2010. Detroit, MI.
5. Wang, J., *PVT properties of polymers for injection molding.* Some critical issues for injection molding, 2012: p. 3-30.
6. Wang, J., et al., *Modeling of pvT behavior of semi-crystalline polymer based on the two-domain Tait equation of state for injection molding.* Materials & Design, 2019. **183**: p. 108149.
7. Rännar, L.-E., *On optimization of injection molding cooling.* 2008.
8. Zuidema, H., G. Peters, and H. Meijer, *Influence of cooling rate on pVT-data of semicrystalline polymers.* Journal of Applied Polymer Science, 2001. **82**(5): p. 1170-1186.
9. Saifullah, A. and S.H. Masood. *An Investigation on Warpage Analysis in Plastic Injection Moulding*. in *Advanced Materials Research*. 2011. Trans Tech Publ.
10. Jacques, M.S., *An analysis of thermal warpage in injection molded flat parts due to unbalanced cooling.* Polymer Engineering & Science, 1982. **22**(4): p. 241-247.
11. Parlevliet, P.P., H.E. Bersee, and A. Beukers, *Residual stresses in thermoplastic composites—A study of the literature—Part I: Formation of residual stresses.* Composites Part A: Applied Science and Manufacturing, 2006. **37**(11): p. 1847-1857.
12. Depolo, W.S. and D. Baird, *Flow-induced warpage of injection-molded TLCP fiber-reinforced polypropylene composites.* Polymer composites, 2006. **27**(3): p. 239-248.
13. Frados, J., *Plastics Engineering Handbook of the Society of the Plastics Industry, Inc.* 1976: Van Nostrand Reinhold.
14. Kim, H.-S., et al., *Effects of Molding Condition on Surface Unevenness of GFRP Composites in Compression Molding.* Transactions of the Korean Society of Mechanical Engineers A, 2010. **34**(11): p. 1649-1657.
15. Bushko, W.C. and V.K. Stokes, *Solidification of thermoviscoelastic melts. Part II: Effects of processing conditions on shrinkage and residual stresses.* Polymer Engineering & Science, 1995. **35**(4): p. 365-383.
16. Bernath, A., *Numerical prediction of curing and process-induced distortion of composite structures*. 2020: Karlsruher Institut für Technologie (KIT).
17. Bian, X., et al., *Effect of water absorption on the behavior of E-glass fiber/nylon-6 composites.* Polymer Composites, 1991. **12**(5): p. 333-337.
18. Pai, C.C., et al., *Effects of moisture on thermal and mechanical properties of nylon-6, 6.* Advances in Polymer Technology: Journal of the Polymer Processing Institute, 1989. **9**(2): p. 157-163.

19. Wang, Y., et al., *Research on the Molding Design and Optimization of the Molding Process Parameters of the Automobile Trunk Trim Panel.* Advances in Materials Science and Engineering, 2020. **2020**.

20. Mukras, S.M., H.M. Omar, and F.A. al-Mufadi, *Experimental-based multi-objective optimization of injection molding process parameters.* Arabian Journal for Science and Engineering, 2019. **44**(9): p. 7653-7665.

21. Martin, E.J., *Evaluation of Warpage for Composite Automotive Components*, in *Faculty of Engineering*. 2020, University of Western Ontario: London, CA.

22. Hwang, S. and J. Kim, *Injection mold design of reverse engineering using injection molding analysis and machine learning.* Journal of Mechanical Science and Technology, 2019. **33**(8): p. 3803-3812.

23. Fu, J. and Y. Ma, *Mold modification methods to fix warpage problems for plastic molding products.* Computer-Aided Design and Applications, 2016. **13**(1): p. 138-151.

24. Lebrun, G. and J. Denault, *Effect of annealing on the thermal expansion and residual stresses of bidirectional thermoplastic composite laminates.* Composites Part A: Applied Science and Manufacturing, 2010. **41**(1): p. 101-107.

25. Parlevliet, P.P., H.E. Bersee, and A. Beukers, *Residual stresses in thermoplastic composites–a study of the literature. Part III: Effects of thermal residual stresses.* Composites Part A: Applied Science and Manufacturing, 2007. **38**(6): p. 1581-1596.

26. Krause, W., et al. *Development of a technology for large scale production of continuous fiber reinforced thermoplastic composites*. in *SPE-Conference, Boston*. 2005.

27. Fengler, B., A. Hrymak, and L. Kärger, *Multi-objective CoFRP patch optimization with consideration of manufacturing constraints and integrated warpage simulation.* Composite Structures, 2019. **221**: p. 110861.

28. Heer, N., et al., *Versatility of Long Fiber AP Nylon CR-6 Organosheet to overcome intrinsic*

short comings of Long Fiber Thermoplastics, in *ACCE Conference*, S.o.P. Engineers, Editor. 2020: Novi, MI.

29. Goris, S., et al., *A novel fiber length measurement technique for discontinuous fiber-reinforced composites: A comparative study with existing methods.* Polymer Composites, 2018. **39**(11): p. 4058-4070.

30. Fisa, B., *Mechanical degradation of glass fibers during compounding with polypropylene.* Polymer composites, 1985. **6**(4): p. 232-241.

31. Stade, K., *Techniques for compounding glass fiber-reinforced thermoplastics.* Polymer Engineering & Science, 1977. **17**(1): p. 50-57.

32. Polini, W., et al., *Measurement of high flexibility components in composite material: critical issues and possible solutions.* The International Journal of Advanced Manufacturing Technology, 2019. **103**(1-4): p. 1529-1542.

33. Javaid, M., et al., *Industrial perspectives of 3D scanning: features, roles and it's analytical applications.* Sensors International, 2021. **2**: p. 100114.

34. Ameen, W., A.M. Al-Ahmari, and S. Hammad Mian, *Evaluation of handheld scanners for automotive applications.* Applied Sciences, 2018. **8**(2): p. 217.

35. Cuesta, E., et al., *Metrological evaluation of laser scanner integrated with measuring arm using optical feature-based gauge.* Optics and Lasers in Engineering, 2019. **121**: p. 120-132.

36. Iuliano, L., P. Minetola, and A. Salmi, *Proposal of an innovative benchmark for comparison of the performance of contactless digitizers.* Measurement Science and Technology, 2010. **21**(10): p. 105102.

37. Martin, E., et al. *Quantitative Characterization of Warpage for Composite Components*. in *CAD'21*. Barcelona: Computer-Aided Design and Applications.

38. Albert, C. and G. Fernlund, *Spring-in and warpage of angled composite laminates.* Composites Science and Technology, 2002. **62**(14): p. 1895-1912.

39. Bula, K., et al., *The use of IR thermography to show the mold and part temperature evolution in injection molding.* Archives of Mechanical Technology and Materials, 2016. **36**(1): p. 40-43.

40. Schwalme, G., *Inline infrared thermography applied for quality gates and for mould temperature control in the injection moulding process*. 2014: Universitätsbibliothek Ilmenau.

41. Whiteside, B., et al. *Ultrasonic injection moulding: A study of thermal behaviour and nanofeature replication*. in *Proceedings of the 16th International Conference of the European Society for Precision Engineering and Nanotechnology, Nottingham, UK*. 2016.

42. Lin, Y.-W., et al., *3D numerical simulation of transient temperature field for lens mold embedded with heaters.* International communications in heat and mass transfer, 2005. **32**(9): p. 1221-1230.

43. Miller, K. and K. Ramani, *Analysis of an inductively heated compression molding process.* Advances in Polymer Technology: Journal of the Polymer Processing Institute, 1998. **17**(3): p. 251-257.

44. Taimarov, M., F. Garifullin, and K. Rusev, *Directional emissivity of structural materials.* Journal of engineering physics, 1986. **49**(2): p. 939-942.

45. Litwa, M., *Influence of angle of view on temperature measurements using thermovision camera.* IEEE Sensors Journal, 2010. **10**(10): p. 1552-1554.

46. Muniz, P.R., S.P. Cani, and R.d.S. Magalhaes, *Influence of field of view of thermal imagers and angle of view on temperature measurements by infrared thermovision.* IEEE Sensors Journal, 2013. **14**(3): p. 729-733.

47. Bergman, T.L., et al., *Fundamentals of heat and mass transfer*. 2011: John Wiley & Sons.

48. Nunak, T., et al. *Thermal image resolution on angular emissivity measurements using infrared thermography*. in *Proceedings of the International MultiConference of Engineers and Computer Scientists*. 2015.

49. NHTSA, *Federal Register*. 2012. p. 62623-63200.

50. Kim, H.J., et al., *Greenhouse Gas emissions payback for lightweighted vehicles using aluminum and high-strength steel.* Journal of Industrial Ecology, 2010. **14**(6): p. 929-946.

51. Stewart, R., *Rebounding automotive industry welcome news for FRP.* Reinforced Plastics, 2011. **55**(1): p. 38-44.

52. Maia, T.D.O., *Finite Element Analysis of Assembly for Warped Composite Automotive Components*, in *Faculty of Engineering*. 2021, University of Western Ontario: London, CA.

53. *Ti401 PRO, Ti480 PRO, TiX501*

and TiX580 Infrared Cameras. [Datasheet] 2019 [cited 2020 May 10]; Available from: https://dam-assets.fluke.com/s3fs-public/6012099a-en-ti401-tix501-ds-w.pdf?lL9b8ezj.RP56TUS0Zu2DVP_bVjGiTze.

54. Moldex3D. *Moldex3D R17 Help*. 2019 [cited 2020; Available from: http://support.moldex3d.com/r17/en/index.html.

55. Bower, K.M., *Analysis of Variance (ANOVA) using MINITAB*. Scientific Computing & Instrumentation, 2000. **17**: p. 64-65.

56. Fisher, R.A., *Statistical methods for research workers*, in *Breakthroughs in statistics*. 1992, Springer.

57. Knoerzer, K., R. Buckow, and C. Versteeg, *Adiabatic compression heating coefficients for high-pressure processing–a study of some insulating polymer materials*. Journal of food engineering, 2010. **98**(1): p. 110-119.

58. Casulli, K., et al., *Compression Heating of Selected Polymers During High-Pressure Processing*. Journal of Food Process Engineering, 2017. **40**(2): p. e12417.

59. Que, D.R., *Correlation of Warpage Predicted with Computer Simulation to Actual Warpage for a Glass-Reinforced Nylon Powertrain Part*. 1997, SAE Technical Paper.

60. Wang, J., et al., *Continuous Two-Domain Equations of State for the Description of the Pressure-Specific Volume-Temperature Behavior of Polymers*. Polymers, 2020. **12**(2): p. 409.

61. Martin, E., et al., *Repeatability and Accuracy of Laser Scanning-Based Reverse Engineering for Warped Composite Components*. Computer-Aided Design and Applications, 2021. **18**: p. 1018-1034.

62. Knezevic, D., et al., *Thermographic Analysis of a Long-Fiber Reinforced Thermoplastic Compression Molding Process*. International Journal of Advanced Manufacturing Technology, 2021. **Accepted for publication**

63. *Abaqus Analysis User's Guide, 2016*.

64. *Abaqus Theory Guide, 2016*.

65. *PolyWorks Inspector Reference Guide, 2017*.

66. Wang, Z., et al., *Image quality assessment: from error visibility to structural similarity*. IEEE transactions on image processing, 2004. **13**(4): p. 600-612.

67. Ugural, A.C. and S.K. Fenster, *Advanced mechanics of materials and applied elasticity*. 2011: Pearson Education.

68. Bauchau, O.A. and J.I. Craig, *Euler-Bernoulli beam theory*, in *Structural Analysis*, O.A. Bauchau and J.I. Craig, Editors. 2009, Springer Netherlands: Dordrecht. p. 173-221.

69. Dzulkipli, A.A. and M. Azuddin, *Study of the effects of injection molding parameter on weld line formation*. Procedia engineering, 2017. **184**: p. 663-672.

70. Hobbs, S., *Some observations on the morphology and fracture characteristics of knit lines*. Polymer Engineering & Science, 1974. **14**(9): p. 621-626.

71. Mielewski, D.F., et al., *Weld line morphology of injection molded polypropylene*. Polymer Engineering & Science, 1998. **38**(12): p. 2020-2028.

72. Bousmina, M., et al., *Diffusion at polymer/polymer interfaces probed by rheological tools*. Macromolecules, 1998. **31**(23): p. 8273-8280.

73. Price, F.P., et al. *Polymer/polymer diffusion. I. Experimental technique*. in *Journal of Polymer Science: Polymer Symposia*. 1978. Wiley Online Library.

74.   Nilsson, G., S.P. Fernberg, and L.A. Berglund, *Strain field inhomogeneities and stiffness changes in GMT containing voids.* Composites Part A: Applied Science and Manufacturing, 2002. **33**(1): p. 75-85.

Curriculum Vitae

Name:	David Knezevic
Post-secondary Education and Degrees:	Western University London, Ontario, Canada 2015-2020 B. E. Sc. Mechanical Engineering, with distinction Western University London, Ontario, Canada 2020-2021 M. E. Sc. Mechanical Engineering
Related Work Experience:	Summer Research Assistant Fraunhofer Project Centre Summer 2019 Teaching Assistant Western University 2020-2021 Research Assistant Western University 2020-2021
Honours and Awards:	Natural Sciences and Engineering Research Council (NSERC) Canada Graduate Scholarships – Master's program (2021)
Publications:	Knezevic, D., Tutunea-Fatan, O.R., Gergely R., Okonski, D.A., Ivanov, S., Dörr, D. Thermographic Analysis of a Long-Fiber Reinforced Thermoplastic Compression Molding Process. International Journal of Advanced Manufacturing Technology, 2021. Accepted for publication.